

1 Identification of the Strong Brønsted Acid Site in a Metal-Organic 2 Framework Solid Acid Catalyst

3
4 Christopher A. Trickett,^{1,2,†} Thomas M. Osborn Popp,^{1,2,3†} Ji Su,^{1,2} Chang Yan,⁴ Jonathan
5 Weisberg,¹ Ashfia Huq,⁵ Philipp Urban,^{1,2} Juncong Jiang,^{1,2} Markus J. Kalmutzki,^{1,2} Qingni
6 Liu,^{1,2} Jayeon Baek,^{1,2} Martin P. Head-Gordon,¹ Gabor A. Somorjai,^{1,2} Jeffrey A. Reimer,^{2,3} and
7 Omar M. Yaghi^{1,2,*}

8
9 ¹Department of Chemistry, Kavli Energy NanoSciences Institute at Berkeley, and Berkeley
10 Global Science Institute, University of California-Berkeley, Berkeley, California 94720

11 ²Materials Sciences Division, Lawrence Berkeley National Laboratory, Berkeley, CA 94720

12 ³Department of Chemical and Biomolecular Engineering, University of California, Berkeley,
13 California 94720, USA University of California-Berkeley, Berkeley, California 94720

14 ⁴Department of Chemistry, Stanford University, Stanford, CA 94305

15 ⁵Neutron Scattering Division, Oak Ridge National Laboratory, P.O. Box 2008 MS-6475, Oak
16 Ridge, TN 37831

17
18 †Authors contributed equally

19 *Correspondence to: yaghi@berkeley.edu

20
21 **Abstract:** It remains difficult to understand the surface of solid acid catalysts at the molecular
22 level, despite their importance for industrial catalytic applications. A sulfated zirconium-based
23 metal-organic framework, MOF-808-SO₄, has previously been shown to be a strong solid
24 Brønsted acid material. In this report, we probe the origin of its acidity through an array of
25 spectroscopic, crystallographic, and computational characterization techniques. The strongest
26 Brønsted acid site is shown to consist of a specific arrangement of adsorbed water and sulfate
27 moieties on the zirconium clusters. When a water molecule adsorbs to one zirconium atom, it
28 participates in a hydrogen bond with a sulfate moiety that is chelated to a neighboring zirconium
29 atom; this motif in turn results in the presence of a strongly acidic proton. On dehydration, the
30 material loses its acidity. The hydrated sulfated MOF exhibits good catalytic performance for the
31 dimerization of isobutene (2-methyl-1-propene), achieving 100% selectivity for C₈ products
32 with good conversion efficiency.

33
34 The chemistry at the surface of solid acid catalysts is of vital importance for industrial catalytic
35 applications, yet a precise molecular picture of these surfaces remains elusive. Attempts to obtain
36 a clear view of the Brønsted acid sites in solid acids such as sulfated zirconia have resulted in
37 multiple proposed models, in part due to the difficulty in characterizing the structure of this

38 amorphous material, but also because of wildly variable properties depending on preparation
39 conditions (1-11). Discerning the molecular structures responsible for the activity of solid acid
40 catalysts provides a richer perspective on the functional properties and catalytic mechanisms of
41 these materials, and illuminates the fundamental surface chemistry relating the molecular
42 structures and their functions. Recently, the synthesis of a metal-organic framework (MOF) solid
43 acid catalyst was reported, achieved by treating a Zr-based MOF, MOF-808, with sulfuric acid to
44 yield the solid acid MOF, MOF-808-SO₄, which was shown to be capable of performing several
45 acid-catalyzed reactions (12,13). In this report, we conclusively identify the structure of the
46 strong Brønsted acid site in MOF-808-SO₄, as being a hydrogen bond pair of two species, water
47 and chelating sulfate, adsorbed on the surface of its zirconium clusters, where the acidic proton is
48 arises as a result of the hydrogen bond. We achieve this through a union of crystallographic,
49 spectroscopic, and computational studies. We also show that MOF-808-SO₄ exhibits good
50 activity and selectivity for the dimerization of isobutene to isooctene, and that dehydration of the
51 material significantly reduces the catalytic activity, confirming the role of water as necessary to
52 the strong acidity of the site.

53

54 **Results and Discussion**

55 The preparation of MOF-808-SO₄ was performed by first synthesizing pristine MOF-808
56 (Fig. 1a), Zr₆O₅(OH)₃(BTC)₂(HCOO)₅(OH₂)₂, with a subsequent exchange of the formate ions
57 on the zirconium clusters for sulfate ions simply by washing the MOF in dilute sulfuric acid (12).
58 The MOF-808 backbone is comprised of an octahedron of zirconium atoms that are triply
59 bridged by μ³-O and μ³-OH groups. The formate groups in the pristine structure each bridge two
60 zirconium atoms to form a six-membered belt around the cluster (13). One cluster is connected to
61 six other clusters through benzene tricarboxylate (BTC) linkers, three above and three below the
62 belt of formates, resulting in a framework with spn topology. Once the formate ions are
63 exchanged for sulfate to yield MOF-808-SO₄ (Fig. 1b), these sulfates may take on multiple
64 binding modes and can take one of several positions along the belt interspersed between
65 additional ligated water molecules, resulting in long-range disorder from one cluster to the next.
66 As this disorder is confined to the surface species on the zirconium clusters, the surface of each
67 cluster has a slightly different local molecular ‘decoration,’ (Fig. 1c) while the structural
68 backbone of MOF-808 is still conserved throughout (14-17). Our challenge is to understand the
69 molecular decoration of the zirconium clusters in MOF-808-SO₄ by first identifying the
70 structures that decorate the cluster surface, and from there, discerning which arrangement of
71 decorating structures results in a strong Brønsted acid site.

72 **Understanding the molecular decoration of the zirconium clusters**

73 Elucidating the coordination mode of sulfate is essential for discerning the local
74 structures that exist on the surface of the clusters. From single crystal X-ray diffraction (SXRD)
75 analysis of a crystal in aqueous solution, the sulfate groups are found to be coordinated in both a
76 bridging and chelating mode (Supplementary Fig. 1), with the bridging mode dominating in a 4:1
77 ratio over chelating (Supplementary Section 3). To obtain further insight into what factors
78 control the coordination mode of these ions, selenated MOF-808 (MOF-808-SeO₄) was
79 synthesized in a similar manner to sulfated MOF-808. The MOF-808-SeO₄ framework in
80 aqueous solution was found to possess only one coordination mode for selenate, where selenate
81 bridges two zirconium atoms, suggesting that perhaps the increased atomic radius of selenium

82 enforces the bridging coordination mode. However, upon activation of these two MOFs under
83 dynamic vacuum and heating at 120 °C, both sulfate and selenate were found to have shifted into
84 the chelating mode exclusively. This was confirmed using Rietveld refinement of the samples
85 measured by powder X-ray diffraction (PXRD) in an argon atmosphere. The solid acid nature of
86 MOF-808-SO₄ is only observed following activation at 120 °C, suggesting that the chelating
87 coordination mode of sulfate is a key contributor to its catalytic activity.

88 Quantifying the average molecular formula for MOF-808-SO₄ constrains further the
89 possibilities for ligand disorder on the surface of the zirconium clusters. Here, balancing the
90 charge on the zirconium clusters guides our stoichiometric analysis. Using inductively coupled
91 plasma-optical emission spectroscopy for elemental analysis, 2.3 sulfur atoms per 6 zirconium
92 atoms were found, meaning an average of 2.3 sulfate groups per zirconium cluster. Since each
93 zirconium atom is in the +4 oxidation state, there is an excess of positive charge that is not
94 properly accounted for within the model so far. To probe this, we turned to powder neutron
95 diffraction (PND) to obtain more precise information on the occupancies and thermal ellipsoids
96 of light elements within the framework (Fig. 2a). A sample of MOF-808-SO₄ with deuterated
97 BTC linker was measured at 10 K and 300 K and refined simultaneously against a structure
98 model, revealing a 1:1 ratio of $\mu^3\text{-O}$ to $\mu^3\text{-OH}$ in both independent crystallographic positions
99 within two standard deviations (Supplementary Section 2). An excess of $\mu^3\text{-O}$ is therefore not
100 what balances the excess positive charge. There is substantially more electron density located
101 around the position of the oxygen that connects zirconium to sulfur, O6, which is the same
102 location as coordinated water molecules bound to the cluster in the as-synthesized MOF-808-
103 SO₄. It is noteworthy to mention that the sulfate position could not be located by PND due to the
104 low occupancy and extremely weak neutron scattering factor of sulfur, thus information from
105 PXRD was used in combination with elemental analysis to confirm its presence in this sample.

106 As the only electron density unaccounted for in this model is located at position O6,
107 where water is present in the structure prior to activation, we can infer that balance of the excess
108 positive charge is achieved here by terminal hydroxide, produced by the deprotonation of water
109 molecules. This assumption is plausible considering terminal water molecules bound to
110 zirconium hydroxide clusters have been found to be acidic (18, 19). The position thus accounts
111 for crystallographically superimposed oxygen from sulfate groups, hydroxide and water
112 molecules that were not removed during the activation process. This overlap excludes the
113 possibility of determining the precise coordinates of hydroxide, water and sulfate oxygen, but the
114 total occupancy of these species was refined freely, converging to 78.4 ± 1.1%. This corresponds
115 to 9.4 oxygen atoms per cluster, out of a possible 12. Since there must be 4.6 oxygen atoms from
116 2.3 bidentate sulfate groups as found by elemental analysis, and 1.4 hydroxide groups for charge-
117 balancing, this leaves 3.4 ± 0.1 oxygen atoms unaccounted for, and are assigned to ligated water.
118 This was confirmed by thermogravimetric analysis - mass spectrometry (TGA-MS) on the
119 activated sample, which demonstrated the loss of 3.1 water molecules per cluster prior to
120 structure decomposition (Supplementary Fig. 16). The first water signal observed from the mass
121 spectrometer peaked at 143 °C, and indicates water is still present following evacuation and
122 heating. After a small, second water loss event at 236 °C, the structure decomposes at around 350
123 °C. This trend can be explained by considering that losing neutral, terminal water ligands would
124 not collapse the structure, but once the framework is completely dehydrated any further mass
125 loss leads to structure decomposition, as this involves the loss of charged species. Evidence from
126 elemental analysis, PND, ¹H nuclear magnetic resonance (NMR) of the digested MOF and TGA-

127 MS, lead to the average molecular formula of
128 $Zr_6O_4(OH)_4(BTC)_2(SO_4)_{2.3}(OH)_{1.4}(OH_2)_{3.1}(DMF)_{0.4}$ for the activated form of MOF-808-SO₄.

129 **Identifying the strong Brønsted acid site**

130 With the average chemical formula now known, the possible species that decorate each
131 zirconium cluster are constrained, simplifying the task of identifying the Brønsted acid site in
132 MOF-808-SO₄. The potential acidic sources are discussed in turn. Firstly, terminal hydroxide
133 may be eliminated simply because terminal water is present and bound to the cluster in the same
134 manner as hydroxide, with terminal water being known to be more acidic (17,18). Protons on
135 sulfate can also be ruled out since the pH of the solution when the MOF is washed with water
136 following incorporation of sulfate is 3.5, while the pK_{a2} value of sulfuric acid is 1.92 (20).
137 Therefore, sulfate must be fully deprotonated at this stage. A direct comparison between μ^3 -OH
138 and terminal water is not as straightforward; however, we found that the water molecules bound
139 to the framework could be successfully removed by holding the temperature at 220 °C overnight
140 while maintaining crystallinity and porosity. This sample will be hereafter referred to as
141 dehydrated MOF-808-SO₄. If the water molecules are indeed the most acidic species present, the
142 material should lose its strong acid properties upon dehydration.

143 To determine if water molecules are the source of the most acidic protons, we adsorbed
144 trimethylphosphine oxide (TMPO) into MOF-808-SO₄ as a probe of acidity and performed ³¹P
145 solid state NMR with magic angle spinning (MAS). TMPO interacts with Brønsted and Lewis
146 acid sites via the lone pairs on its oxygen atom. Strong acid sites polarize the phosphorus-oxygen
147 bond, resulting in a linear relationship between ³¹P chemical shift values of adsorbed TMPO and
148 the strength of the acid site, where a higher ³¹P chemical shift corresponds to a stronger acid site
149 (21-25). MOF-808-SO₄ with adsorbed TMPO shows a ³¹P resonance at 69 ppm associated with a
150 strongly acidic site (Fig. 2b, i), consistent with what has been previously observed for this
151 material (12). This resonance at 69 ppm is found to be absent when TMPO is used in dehydrated
152 MOF-808-SO₄ (Fig. 2b, ii). As the loss of a water molecule is associated with the loss of the
153 strongest acid site, this result supports the role of terminal water as the strongest Brønsted acid
154 source.

155 At this point, two key molecular features decorating the zirconium clusters have been
156 identified as essential to the acidity of MOF-808-SO₄: the chelating mode of sulfate and terminal
157 water ligand. In isolation, neither of these two species is sufficient to account for the acidity of
158 this MOF, therefore its strong Brønsted acidity must arise from a specific arrangement of these
159 species on the cluster surface. Given the many possible ways to decorate the belt of the cluster
160 with terminal water, terminal hydroxide, and chelating sulfate, several arrangements were chosen
161 to be modeled and geometrically optimized using density functional theory (DFT). The formula
162 $Zr_6O_4(OH)_4(C_2H_3O_2)_6(SO_4)_2(OH)_2(OH_2)_x$ was used as a representation of an average cluster,
163 where $x = 2$ or 3 . The restrictions on structural arrangement of the cluster included (i) the core
164 $[Zr_6O_4(OH)_4(C_2H_3O_2)_6]^{6+}$ being fixed, with μ^3 -O and -OH groups arranged in the commonly
165 reported alternating arrangement to minimize charge repulsion, (ii) modeling sulfate as chelating
166 to zirconium as opposed to bridging, (iii) using terminal hydroxide to charge-balance the cluster,
167 (iv) including two to three water molecules per cluster. Additionally, individual clusters were
168 modeled by truncating the linker with acetate groups, which assumes the clusters are
169 electronically decoupled. The most enlightening result obtained from the different modeled
170 arrangements on the clusters is from the comparison of terminal water in isolation versus
171 adjacent to a chelating sulfate group. An O-H bond length of 0.98 Å was observed on the

172 terminal water molecules that have no significant interactions with neighboring adsorbed
173 molecules. However, when the terminal water molecule is adjacent to chelating sulfate, there is a
174 strong hydrogen bonding interaction, with an O-H bond length ranging from 1.02 – 1.05 Å
175 depending on the particular cluster modeled, significantly longer than the O-H bond with no
176 hydrogen bonding. This is accompanied by an O-H...O angle of 163-166° and a short H...O
177 hydrogen bonding distance of 1.50 – 1.66 Å, indicating that the proton is very weakly bound.
178 Indeed, the system can be viewed as a protonated conjugate of an adsorbed pair of hydroxide and
179 sulfate, with the proton sitting between the two groups but localized mostly on the hydroxide.
180 One example of this site on a modeled cluster is represented in Fig. 3, which was modeled with
181 overall two water molecules and two chelating sulfate groups located on opposite sides of the
182 zirconium cluster.

183 The broken symmetry of the water molecule at this proposed acid site implies that the
184 water participating in a hydrogen bond to chelating sulfate should have distinctly different
185 spectroscopic signatures for its two proton environments. We will refer to these two sites as H_a
186 for the acidic proton on water participating in the hydrogen bond to chelating sulfate, and H_b for
187 the other proton pointing into free space. To probe these proton chemical environments directly,
188 we performed ¹H solid state NMR. Fig. 4a shows the ¹H MAS spectrum of MOF-808-SO₄ at 6
189 kHz MAS taken before and after dehydration, and their difference. The difference spectrum
190 shows that two peaks at around 2.5 ppm and 8.1 ppm are lost as a result of dehydration.
191 Assigning the identity of these resonances is informed by comparing to the DFT-calculated ¹H
192 NMR chemical shifts of two of the modeled zirconium clusters (Section S7, Tables S4 and S5).
193 The difference in chemical shift ($\Delta\delta$) between the H_a and H_b protons in the acid site is calculated
194 for two cases to be $\Delta\delta = 5.1$ ppm and $\Delta\delta = 9.1$ ppm. Water lacking a strong hydrogen bonding
195 interaction to chelating sulfate is calculated to have only $\Delta\delta = 2.0$ ppm between the two protons.
196 The changes in the spectra in Fig. 4a after dehydration suggest that the two lost resonances
197 belong to the H_a and H_b protons on the water molecule in the acid site with $\Delta\delta = 5.6$ ppm, where
198 H_a, the acidic proton, is the downfield resonance.

199 In order to confirm that these two resonances are the H_a and H_b protons belonging to the
200 same water molecule, a rotor-synchronized double-quantum (DQ) MAS NMR experiment with
201 the back-to-back (BABA) recoupling sequence was performed. This experiment correlates
202 proton resonances in the standard, single-quantum (SQ) spectrum by their proximity to one
203 another through space. A peak in the DQ dimension indicates that a pair of protons is in close
204 enough proximity to generate a double quantum coherence (26). As the closest pairs of protons
205 in MOF-808-SO₄ belong to those on μ^1 -water molecules, we expect these to be the primary
206 coherences observed. The intensity of these peaks is dependent upon the number of duplicate
207 pairs exhibiting this coherence, as well as the efficiency at which this coherence is excited, i.e.
208 the internuclear distance (27). The SQ H_a and H_b resonances at 8.7 ppm 2.5 ppm, respectively,
209 exhibit strong cross peaks at a DQ frequency of 11.2 ppm, indicating their close spatial
210 proximity and confirming that these two resonances must arise from a single water species (Fig.
211 4b). The low-intensity cross peaks between 8.7 and 3.1 ppm may arise from a small subset of H_a
212 and H_b protons in acid sites with a slightly different local arrangement of nearest neighbor μ^1 -OH
213 and μ^3 -OH groups. Along the diagonal, a strong autocorrelation DQ peak at around 5.0 ppm is
214 observed for an SQ resonance at around 2.5 ppm, which arises from pairs of protons belonging to
215 isolated terminal water at other sites on the zirconium cluster. The chemical environment of the
216 protons on water molecules not neighboring a chelating sulfate is similar to the chemical
217 environment of the H_b proton in the acid site, and accordingly, their chemical shifts should be

218 similar. This is supported by our DFT calculations, where the chemical shifts of protons in these
219 environments were calculated to be within about ± 1 ppm of one another. The ^1H solid state
220 NMR results reveal a picture consistent with the proposed molecular conformation of the
221 Brønsted acid site, where water hydrogen-bonded to sulfate has two protons with inequivalent O-
222 H bond lengths and inequivalent chemical shifts. The subsequent loss of these peaks after
223 dehydration at 220 °C is correlated with a loss of acidity, resulting in the conclusion that the
224 strong Brønsted acid site arises from this hydrogen bonding interaction between water and
225 chelating sulfate.

226 **Removal of water at the acid site impacts catalytic performance**

227 These results suggest a structure-property relationship in MOF-808-SO₄, where water
228 must be present and adjacent to chelating sulfate to yield strong acidity. We sought to test this
229 hypothesis by measuring the activity of MOF-808-SO₄ in catalyzing the dimerization of
230 isobutene (2-methylprop-1-ene), and to see whether removing the water molecule in the active
231 site by dehydration would affect this activity. The dimerization of isobutene may yield two
232 products, either 2,4,4-trimethyl-1-pentene or 2,4,4-trimethyl-2-pentene, both referred to as
233 isooctene (Fig. 5a). The terminal alkene product is prized as a starting material for synthesizing
234 terminal aldehydes and alcohols, but both alkene products may be hydrogenated to form 2,4,4-
235 trimethylpentane, known as isooctane, a valuable gasoline octane booster (28-30). In the process
236 of dimerizing isobutene, higher order alkene oligomer products greater than C8 may form, which
237 is typically disfavored, as a separation step is required to isolate the C8 species. Selectivity for
238 C8 products is crucial if isooctane is the desired product (31,32). To that end, MOF-808-SO₄ was
239 benchmarked against other solid acid catalysts for C8 selectivity and conversion efficiency
240 (sulfated zirconia, Amberlyst, and H-ZSM-5) using a continuous gas flow setup, with isobutene
241 diluted in helium and at atmospheric pressure (Supplementary Section 11). The advantage of
242 using a gas flow setup over a solvent-based process is that it allows for continuous production,
243 and negates the need to purify isooctene from solvent mixtures. Our benchmark materials were
244 chosen based on their capacity to operate under these conditions, and their catalytic activities
245 were evaluated with respect to the mass of the catalyst. MOF-808-SO₄ was found to be active
246 even at room temperature, with conversion peaking at 160 °C at 21.5%, outperforming
247 Amberlyst, sulfated zirconia and H-ZSM-5 under these conditions (Fig. 5b). The C8 selectivity
248 of MOF-808-SO₄ is found to be 100% at 80 °C and lower, yet remains at 92.8% at 160 °C,
249 similar to sulfated zirconia (Fig. 5c). The C8 product distribution for both MOF-808-SO₄ and
250 sulfated zirconia runs about 4:1 in favor of the terminal alkene product (Supplementary Figs. 28-
251 30). H-ZSM-5 and Amberlyst exhibit C8 selectivity under 35% at all temperatures, forming a
252 mixture of many different higher order oligomers. Though the C8 selectivity and product
253 distribution for MOF-808-SO₄ and sulfated zirconia are comparable, under longer experiments of
254 up to 15 days at 80 °C, MOF-808-SO₄ does not lose activity or selectivity, maintaining a
255 constant 15% conversion while the conversion efficiency of sulfated zirconia drops by around
256 60% from its starting value of 5.2% (Fig. 5d). MOF-808-SO₄ does begin lose activity at 120 °C
257 and 160 °C, and at a faster rate with increasing temperature, consistent with the notion that
258 desorption of water from the zirconium clusters at higher temperatures should affect the
259 Brønsted acid site. Indeed, when dehydrated MOF-808-SO₄ was tested as a catalyst, the
260 conversion was found to be 80 % less than that of MOF-808-SO₄ at 80 °C (Fig. 5b). The great
261 majority of the catalytic activity of the material can thus be attributed to this acid site, where
262 water is adjacent and hydrogen bonded to chelating sulfate. The C8 selectivity and product

263 distribution for dehydrated MOF-808-SO₄ are almost identical to that of MOF-808-SO₄ and
264 sulfated zirconia, indicating that this acid site alone is not responsible for the selectivity.

265 We conclude that perturbing the strong Brønsted acid site by removing the water adjacent
266 to chelating sulfate has a significant negative impact on the catalytic performance of MOF-808-
267 SO₄. The remaining activity of the material in the absence of this water molecule suggests that
268 Lewis acid sites in the material may also contribute to its activity but to a lesser extent, a
269 possibility supported by the observation of open metal sites in the PND refinement of the
270 structure (Supplementary Section 2). Regeneration of the catalyst thus only requires replacing
271 the water molecule adjacent to sulfate, which can be done by repeating the solvent exchange and
272 activation process. Future work may find a more efficient process whereby the catalyst is
273 regenerated continuously during operation by the addition of water vapor into the product
274 stream, maintaining the active site even at higher temperatures.

275 The relative strength of this acid site compared to other acids is of interest, as its structure
276 may serve as a model for the design of new strong acid sites. While MOF-808-SO₄ has been
277 previously stated to be superacidic by colorimetric methods (12), these methods can sometimes
278 prove unreliable for acid sites existing at the interface of the solid and gas phase (33). We can
279 provide a thermodynamically-based estimate of the acidity of this specific Brønsted acid site
280 based on a previously calculated relationship between the ³¹P chemical shift of adsorbed TMPO
281 and the deprotonation energy of simulated Brønsted acid sites (20,21). The TMPO resonance at
282 69 ppm correlated to the acid site in this material corresponds to a deprotonation energy of 1214
283 kJ/mol. It is generally accepted that a superacid is a medium in which the chemical potential of
284 the proton is higher than in sulfuric acid (34). The deprotonation energy for gas-phase sulfuric
285 acid has been experimentally determined to be 1295 kJ/mol (35), which suggests that this
286 Brønsted site in MOF-808-SO₄ is at the very least comparable to sulfuric acid, and may even be
287 considered superacidic by this measure. At its core, the structure of this site in MOF-808-SO₄ is
288 characterized by the pairing of two bases (chelating sulfate and μ¹-OH) supported on two
289 neighboring zirconium atoms and sharing a weakly bound proton between them. Thus such a
290 Brønsted acid site construct may be quite generalizable, as it may be possible to reduce the
291 deprotonation energy of this proton to yield even stronger acidity by manipulating the identities
292 of these two bases or of the support atoms.

293
294 **Data availability.** Synthetic and experimental procedures, as well as crystallographic, spectroscopic
295 and computational data are provided in the Supplementary Information. All other data are available
296 from the authors upon reasonable request.

297

298 **References**

299

- 300 1. Arata, K. Solid Superacids. *Adv. Catal.* **37**, 165 (1990).
- 301 2. Ward, D. A. & Ko, E. I. One-Step Synthesis and Characterization of Zirconia-Sulfate
302 Aerogels as Solid Superacids. *J. Catal.* **150**, 18–33 (1994).
- 303 3. Haase, F. & Sauer, J. The Surface Structure of Sulfated Zirconia: Periodic ab Initio Study
304 of Sulfuric Acid Adsorbed on ZrO₂(101) and ZrO₂(001). *J. Am. Chem. Soc.* **120**, 13503–
305 13512 (1998).
- 306 4. Bensitel, M., Saur, O., Lavalley, J.C., & Morrow, B. A. An infrared study of sulfated

- 307 zirconia. *Mater. Chem. Phys.* **19**, 147–156 (1988).
- 308 5. Clearfield, A., Serrette, G. P. D., & Khazi-Syed, A. H. Nature of hydrous zirconia and
309 sulfated hydrous zirconia. *Catal. Today.* **20**, 295–312 (1994).
- 310 6. Kustov, L. M., Kazansky, V. B., Figueras, F., & Tichit, D. Investigation of the Acidic
311 Properties of ZrO₂ Modified by SO₄²⁻ Anions. *J. Catal.* **150**, 143–149 (1994).
- 312 7. Adeeva, V. et al. Acid sites in sulfated and metal-promoted zirconium dioxide catalysts. *J.*
313 *Catal.* **151**, 364–372 (1995).
- 314 8. Bolis, V., Magnacca, G., Cerrato, G., & Morterra, C., Microcalorimetric characterization
315 of structural and chemical heterogeneity of superacid SO₄/ZrO₂ systems. *Langmuir.* **13**,
316 888–894 (1997).
- 317 9. Hino, M., Kurashige, M., Matsushashi, H., & Arata, K. The surface structure of sulfated
318 zirconia: Studies of XPS and thermal analysis. *Thermochim. Acta.* **441**, 35–41 (2006).
- 319 10. Arata, K. Organic syntheses catalyzed by superacidic metal oxides: sulfated zirconia and
320 related compounds. *Green Chem.* **11**, 1719–1728 (2009).
- 321 11. Yadav, G. D. & Nair, J. J. Sulfated zirconia and its modified versions as promising
322 catalysts for industrial processes. *Microporous Mesoporous Mater.* **33**, 1–48 (1999).
- 323 12. Jiang, J. et al. Superacidity in Sulfated Metal – Organic Framework-808. *J. Am. Chem.*
324 *Soc.* **136**, 12844–12847 (2014).
- 325 13. Furukawa, H. et al. Water adsorption in porous metal-organic frameworks and related
326 materials. *J. Am. Chem. Soc.* **136**, 4369–81 (2014).
- 327 14. Osborn Popp, T. M. & Yaghi, O.M. Sequence-Dependent Materials. *Acc. Chem. Res.* **50**,
328 532–534 (2017).
- 329 15. Cairns, A. B. & Goodwin, A. L. Structural disorder in molecular framework materials.
330 *Chem. Soc. Rev.* **42**, 4881–93 (2013).
- 331 16. Furukawa, H., Müller, U., & Yaghi, O. M. “Heterogeneity within order” in metal-organic
332 frameworks. *Angew. Chem. Int. Ed.* **54**, 3417–3430 (2015).
- 333 17. Trickett, C. A. et al. Definitive molecular level characterization of defects in UiO-66
334 crystals. *Angew. Chem. Int. Ed.* **54**, 11162–11167 (2015).
- 335 18. Åberg, M. & Glaser, J. ¹⁷O and ¹H NMR study of the tetranuclear hydroxo zirconium
336 complex in aqueous solution. *Inorg. Chim. Acta.* **206**, 53–61 (1993).
- 337 19. Springborg, J. Hydroxo-Bridged Complexes of Chromium (III), Cobalt (III), Rhodium
338 (III), and Iridium (III). *Adv. Inorg. Chem.* **32**, 55–169 (1988).
- 339 20. Hall, J. *Lab Manual for Zumdahl/Zumdahl’s Chemistry*, p. 656, (2002).
- 340 21. Zheng, A., Zhang, H., Lu, X., Liu, S. B., & Deng, F. Theoretical predictions of ³¹P NMR
341 chemical shift threshold of trimethylphosphine oxide adsorbed on solid acid catalysts. *J.*
342 *Phys. Chem. B* **112**, 4496–4505 (2008).
- 343 22. Zheng, A. et al. ³¹P Chemical Shift of Adsorbed Trialkylphosphine Oxides for Acidity
344 Characterization of Solid Acids Catalysts. *J. Phys. Chem.* **112**, 7349–7356 (2008).

- 345 23. Zheng, A., Huang, S.J., Liu, S. B., & Deng, F. Acid properties of solid acid catalysts
346 characterized by solid-state ^{31}P NMR of adsorbed phosphorous probe molecules. *Phys.*
347 *Chem. Chem. Phys.* **13**, 14889 (2011).
- 348 24. Chen, W. H. et al. A solid-state NMR, FT-IR and TPD study on acid properties of sulfated
349 and metal-promoted zirconia: Influence of promoter and sulfation treatment. *Catal. Today.*
350 **116**, 111–120 (2006).
- 351 25. Lunsford, J. H., Sang, H., Campbell, S. M., Liang, C. H., & Anthony, R. G. An NMR
352 study of acid sites on sulfated-zirconia catalysts using trimethylphosphine as a probe.
353 *Catal. Letters.* **27**, 305–314 (1994).
- 354 26. Gottwald, J., Demco, D. E., Graf, R., & Spiess, H. W. High-resolution double-quantum
355 NMR spectroscopy of homonuclear spin pairs and proton connectivities in solids. *Chem.*
356 *Phys. Lett.* **243**, 314–323 (1995).
- 357 27. Schnell, I., Brown, S. P., Low, H. Y., Ishida, H., & Spiess, H. W. An investigation of
358 hydrogen bonding in benzoxazine dimers by fast magic-angle spinning and double-
359 quantum ^1H NMR spectroscopy. *J. Am. Chem. Soc.* **120**, 11784–11795 (1998).
- 360 28. Mahdi, H. I. & Muraza, O. Conversion of isobutylene to octane-booster compounds after
361 methyl tert-butyl ether phaseout: The role of heterogeneous catalysis. *Ind. Eng. Chem.*
362 *Res.* **55**, 11193–11210 (2016).
- 363 29. Takahashi, K., Yamashita, M., & Nozaki, K. Tandem hydroformylation/hydrogenation of
364 alkenes to normal alcohols using Rh/Ru dual catalyst or Ru single component catalyst. *J.*
365 *Am. Chem. Soc.* **134**, 18746–18757 (2012).
- 366 30. Behr, A. *Ullman's Encyclopedia of Industrial Chemistry*. 223–269 (2010).
- 367 31. Izquierdo, J. F., Vila, M., Tejero, J., Cunill, F., & Iborra, M., Kinetic study of isobutene
368 dimerization catalyzed by a macroporous sulphonic acid resin. *Appl. Catal. A, Gen.* **106**,
369 155–165 (1993).
- 370 32. Kamath, R. S., Qi, Z., Sundmacher, K., Aghalayam, P., & Mahajani, S. M. Process
371 analysis for dimerization of isobutene by reactive distillation. *Ind. Eng. Chem. Res.* **45**,
372 1575–1582 (2006).
- 373 33. Song, X. & Sayari A. Sulfated zirconia-based strong solid-acid catalysts: recent progress.
374 *Cat. Rev.* **38**, 329-412 (1996).
- 375 34. Himmel, D., Goll, S.K., Leito, I., & Krossing, I., A unified pH scale for all phases, *Angew.*
376 *Chem. Int. Ed.* **49**, 6885-6888, (2010).
- 377 35. Viggiano, A. A., Henschman, M. J., Dale, F., Deakyne, C. A., & Paulson, J. F. Gas-phase
378 reactions of weak Brønsted bases I^- , PO_4^- , HSO_4^- , FSO_3^- , and CF_3SO_3^- with strong Brønsted
379 acids H_2SO_4 , FSO_3H , and $\text{CF}_3\text{SO}_3\text{H}$, A quantitative intrinsic superacidity scale for the
380 sulfonic acids XSO_3H ($\text{X} = \text{HO}, \text{F}, \text{and CF}_3$). *J. Am. Chem. Soc.* **114**, 4299-4306, (1992).

381

382 Acknowledgements

383 This work, including synthesis, characterization and crystal structure analysis was funded by
384 BASF SE (Ludwigshafen, Germany) and the U.S. Department of Defense, Defense Threat
385 Reduction Agency (HDTRA 1-12-1-0053). Work performed at the Advanced Light Source is

386 supported by the Director, Office of Science, Office of Basic Energy Sciences, of the U.S.
387 Department of Energy under Contract No. DE-AC02-05CH11231. A portion of this research
388 used resources at the Spallation Neutron Source, a DOE Office of Science User Facility operated
389 by the Oak Ridge National Laboratory. NMR work was supported as part of the Center for Gas
390 Separations Relevant to Clean Energy Technologies, an Energy Frontier Research Center funded
391 by the U.S. Department of Energy, Office of Science, Basic Energy Sciences under Award # DE-
392 SC0001015. T.O.P. acknowledges funding from the NSF Graduate Research Fellowship
393 Program. C.Y. acknowledges support from a Hewlett-Packard Stanford Graduate Fellowship.
394 P.U. acknowledges the German Research Foundation (DFG, PU 286/1-1). M.J.K is grateful for
395 financial support through the German Research Foundation (DFG, KA 4484/1-1). We
396 acknowledge Bunyarat Rungtaweivoranit for his assistance with electron microscopy; Simon
397 Teat and Laura McCormick for the synchrotron X-ray diffraction data acquisition support at
398 beamline 11.3.1 of the Advanced Light Source, Lawrence Berkeley National Laboratory.

399

400 **Author Contributions**

401 C.T. and T.O.P co-wrote the manuscript. C.T. performed the PND modeling, SXR and PXR
402 experiments. T.O.P. performed the solid state NMR experiments and NMR DFT calculations,
403 with support and advice from J.R. J.S., Q.L. and J.B. performed the dimerization catalysis
404 experiments with the support and advice of G.S. C.Y. performed the IR experiments. J.W.
405 performed the DFT calculations on the cluster models, with support and advice from M.H.G.
406 A.H. performed the PND experiments. P.U. performed the PXR Rietveld refinements. M.K.
407 helped with TGA experiments. J.J. supported and advised the synthesis. O.Y. supervised the
408 project. All authors reviewed and edited the manuscript and contributed useful discussions.

409

410 **Competing interests**

411 The authors declare no competing interests.

412

413

414 **Additional information**

415 Supplementary information is available in the online version of the paper. Reprints and
416 permissions information is available online at www.nature.com/reprints.

417

418 Correspondence and requests for materials should be addressed to O.Y.

419

420

421 **Figure Captions**

422

423 **Fig. 1. MOF-808, MOF-808-SO₄, and visualization of differences in molecular ‘decoration.’**
424 **(a)** Pristine MOF-808 is comprised of 6-connected zirconium-based metal clusters containing
425 five formate groups and linked by benzenetricarboxylate (BTC) into the depicted spn topology
426 framework. These formates may be substituted with sulfate anions as in **(b)**, which coordinate in
427 a bidentate fashion to zirconium, either in chelating mode to a single zirconium atom, or in a
428 bridging mode to two zirconium atoms. Sulfate is predominantly in the bridging mode in the
429 solvated MOF, and converts exclusively to the chelating mode following activation by heating
430 under dynamic vacuum. **(c)** Two representations of modeled zirconium clusters, with BTC-
431 linkers omitted beyond the coordinating carboxylate group, highlight the differences in

432 molecular ‘decoration’ between clusters in the overall structure. A similar stoichiometry of
433 hydroxide, water and sulfate groups are present on each cluster, but the local arrangement and
434 apportionment of these groups differs between each cluster.

435 **Fig. 2. Structural characterization of MOF-808-SO₄ by Rietveld refinement of powder**
436 **neutron data, and NMR evidence for presence of water being central to the strong acid site.**
437 **(a)** The data obtained from powder neutron diffraction (red) is compared against the calculated
438 pattern from the structural model (black), and their difference (blue). $wRp = 2.91\%$, $Rp = 9.59\%$.
439 **(b)** ³¹P MAS solid state NMR spectra of trimethylphosphine oxide (TMPO) adsorbed into (i)
440 MOF-808-SO₄ (blue) and (ii) dehydrated MOF-808-SO₄ (red). The peak at 69 ppm, assigned to
441 TMPO interacting with the strong Brønsted acid site, is lost upon dehydration. The peak centered
442 at 42 ppm is due to excess TMPO that is not interacting with acid sites directly. Other peaks in
443 the spectra belong to TMPO adsorbed at various μ^1 -OH, μ^3 -OH, and terminal water sites.

444 **Fig. 3. Depiction of the zirconium cluster and Brønsted acid site in MOF-808-SO₄ as**
445 **determined by DFT geometry optimization. (a)** the overall cluster, **(b)** a close-up view of the
446 acid site with relevant bond lengths and angles, with the acidic proton participating in the
447 hydrogen bond labeled as H_a, and the other as H_b. Atoms not directly part of the active site are in
448 grey, with zirconium in blue, oxygen in red, sulfur in yellow and hydrogen in white.

449 **Fig. 4. Identification of the resonances attributable to adsorbed water using ¹H solid state**
450 **NMR, comparing MOF-808-SO₄ before and after dehydration. (a)** ¹H MAS spectrum of
451 MOF-808-SO₄ at 6 kHz MAS (blue), ¹H MAS spectrum of dehydrated MOF-808-SO₄ at 6 kHz
452 MAS (red), and their difference (black) showing the loss of two prominent peaks assigned as the
453 two inequivalent protons on a water molecule hydrogen-bonded to sulfate. **(b)** ¹H DQ-MAS
454 NMR spectrum of MOF-808-SO₄ with SQ and DQ skyline projections (blue). The spectrum was
455 recorded at 12.5 kHz with two cycles of the BABA recoupling sequence for excitation and
456 reconversion of DQ coherence. The two peaks that are lost upon dehydration appear at 2.5 and
457 8.7 ppm and exhibit a DQ coherence at 11.2 ppm, and are assigned as the inequivalent protons
458 on terminal water hydrogen bonded to chelating sulfate. The prominent peak along the
459 autocorrelation diagonal at 5 ppm is assigned as terminal water elsewhere on the zirconium
460 cluster, not adjacent to sulfate.

461
462
463 **Fig. 5. Comparison of the catalytic conversion, selectivity, and long-term stability of MOF-**
464 **808-SO₄ and dehydrated MOF-808-SO₄ against benchmark catalysts. (a)** General reaction
465 scheme for the dimerization of isobutene (2-methylprop-1-ene) to isooctene (2,4,4-trimethylpent-
466 1-ene, 2,4,4-trimethylpent-2-ene). **(b)** Plot of the percent conversion of isobutene to isooctene for
467 MOF-808-SO₄ (blue), dehydrated MOF-808-SO₄ (red), sulfated zirconia (green), Amberlyst
468 (orange) and H-ZSM-5 (pink) from room temperature up to 200 °C. Amberlyst is the most active
469 at low temperatures while MOF-808-SO₄ has a strong temperature dependence. Dehydrated
470 MOF-808-SO₄ has significantly lower conversion efficiency, indicating that the presence of
471 water adjacent to chelating sulfate is responsible for the majority of the activity. **(c)** Plot of the
472 selectivity for dimer products over higher order oligomers. Both Amberlyst and H-ZSM-5 have
473 poor selectivity, favoring higher order oligomers at all temperatures. MOF-808-SO₄, dehydrated
474 MOF-808-SO₄, and sulfated zirconia have nearly 100% selectivity for dimer products up to 80
475 °C **(d)** Plot of the long-term catalytic performance of MOF-808-SO₄ for the dimerization of

476 isobutene at 80 °C (blue), 120 °C (violet) and 160 °C (dark red), against sulfated zirconia (green)
477 at 80 °C. The conversion efficiency for MOF-808-SO₄ is maintained at 80 °C, but at higher
478 temperatures the material loses activity with an increasing rate, likely due to desorption of
479 terminal water from the clusters at these temperatures. Sulfated zirconia at 80 °C has
480 approximately one third of the activity of MOF-808-SO₄ at 80 °C, but falls to about half this
481 value by 240 hours, while MOF-808-SO₄ maintains its conversion level throughout this period.

Table of contents graphic:

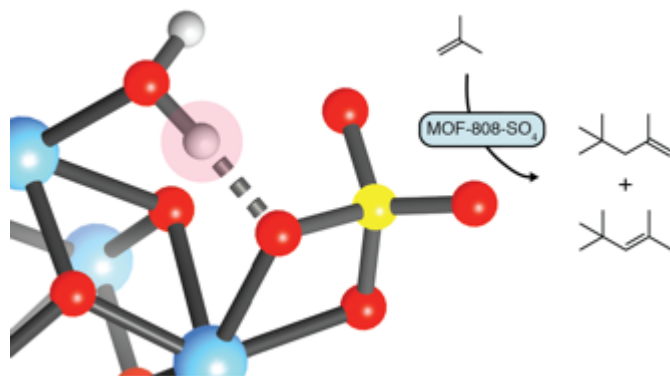


Figure 1:

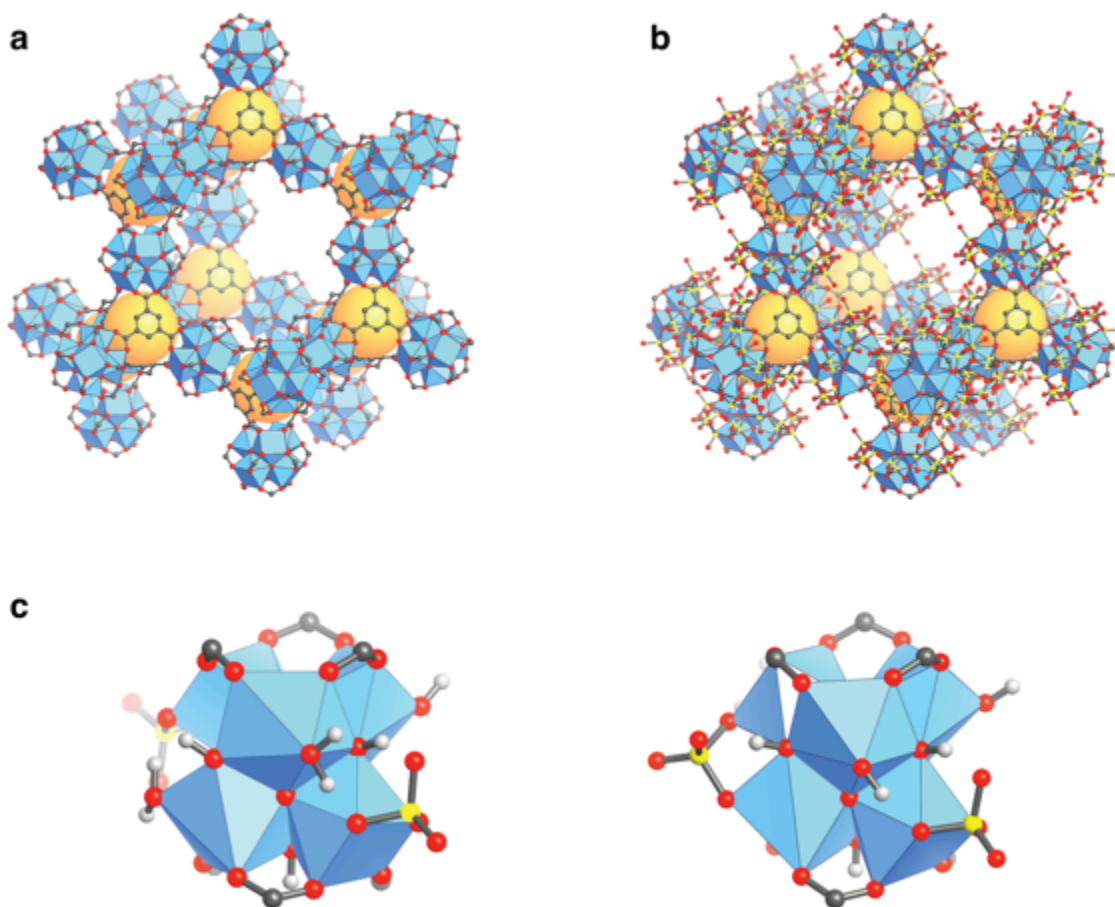


Figure 2:

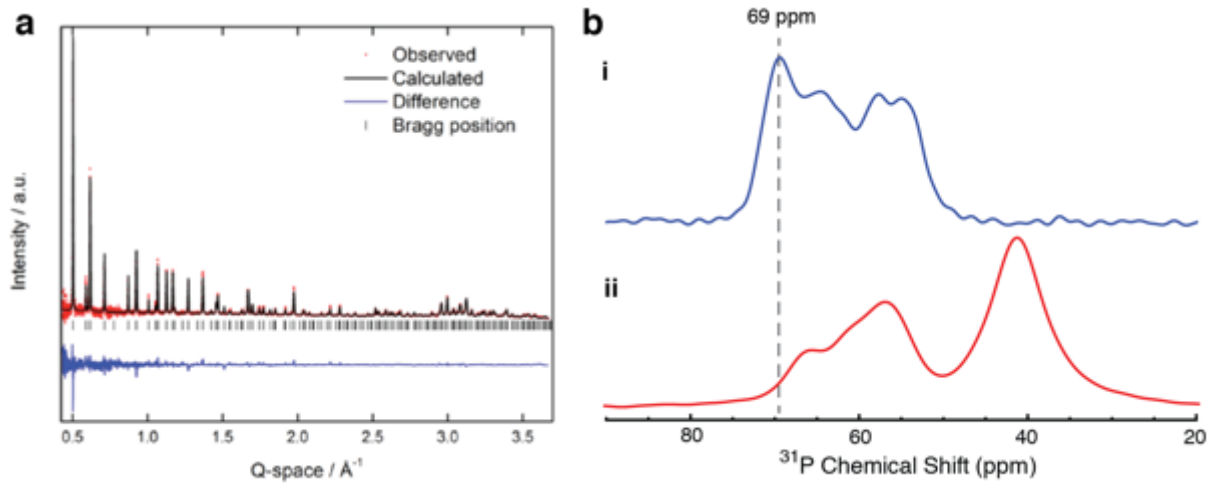


Figure 3:

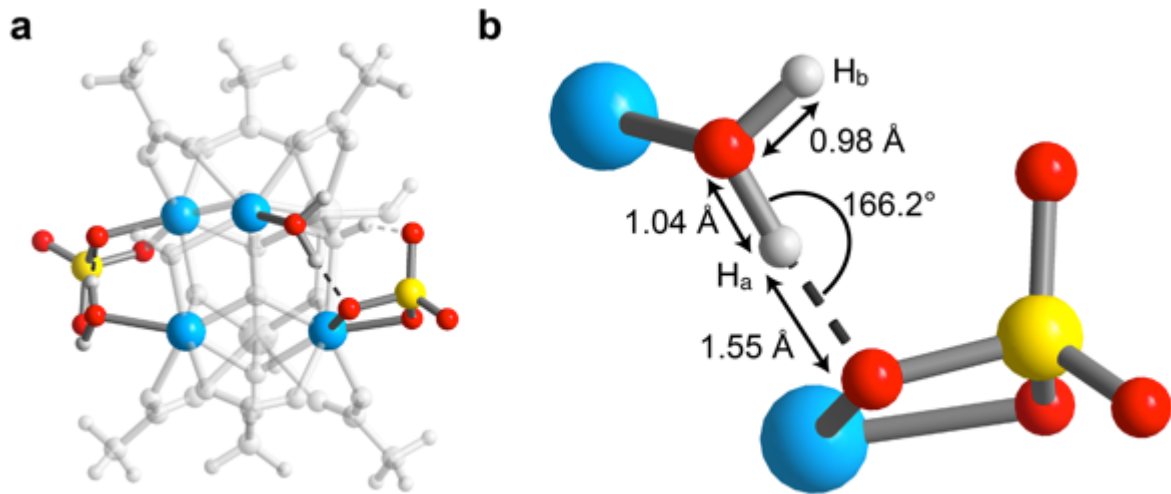


Figure 4:

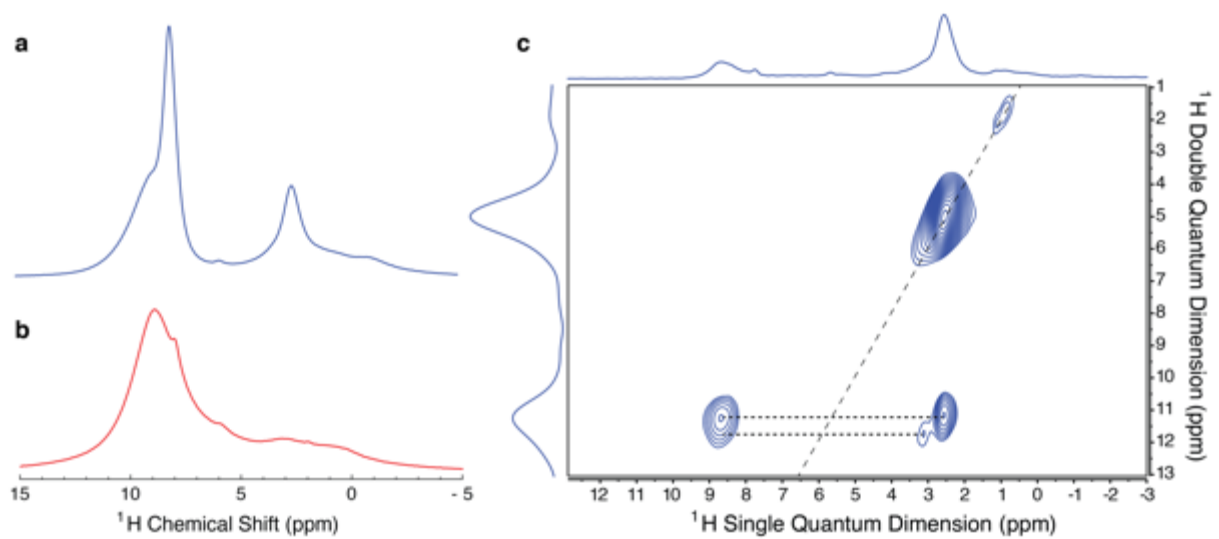
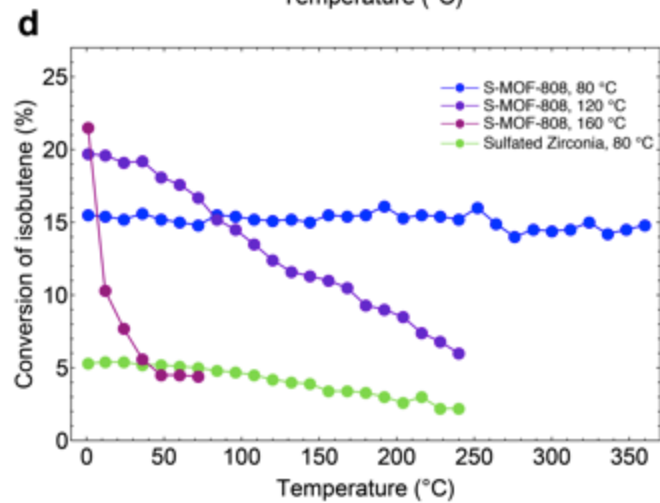
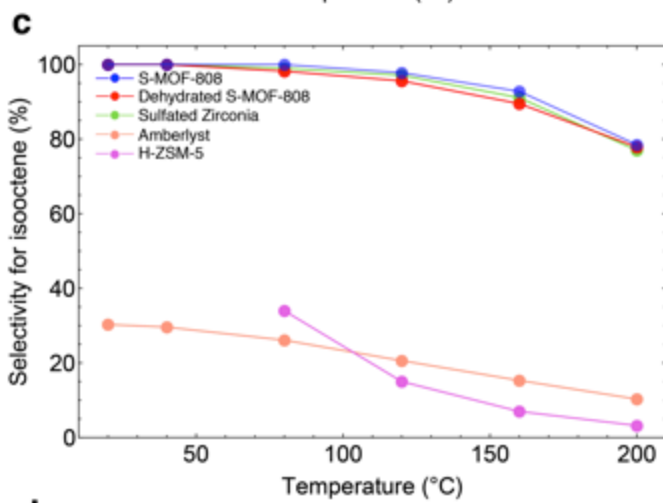
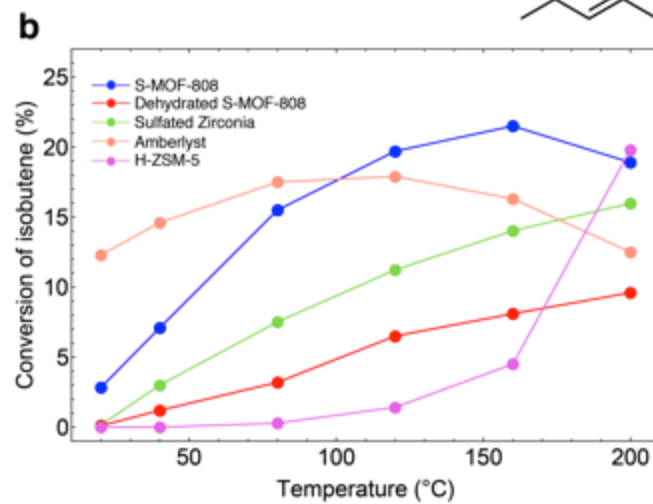
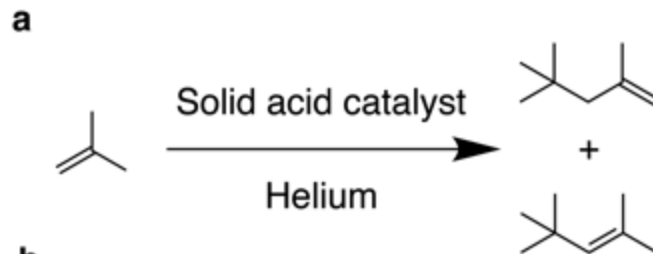


Figure 5:



Supplementary Information

Identification of the Strong Brønsted Acid Site in a Metal-Organic Framework Solid Acid Catalyst

Table of Contents

Section 1: Syntheses of Materials	2
Section 2: Powder Neutron Diffraction Experiments	4
Section 3: Single Crystal X-ray Diffraction Analyses	12
Section 4: Powder X-ray Diffraction Patterns, Rietveld	18
Section 5: Thermogravimetric Analysis	25
Section 6: N ₂ Sorption Isotherms	28
Section 7: Solid State NMR Spectroscopy	31
Section 8: <i>In Situ</i> Infrared Spectroscopy	36
Section 9: Scanning Electron Microscopy	42
Section 10: Cluster Geometry Optimization	42
Section 11: Acid Catalysis of Isobutene	44
Section 12: References	44

Section 1: Syntheses of Materials

Methods.

Chemicals used in this work. *N,N*-dimethylformamide (DMF) was obtained from Fisher Scientific. Formic acid (purity > 98%) and anhydrous chloroform were obtained from EMD Millipore Chemicals. Anhydrous acetone was obtained from Acros Organics. Zirconium oxychloride octahydrate (>99.5%), hydrofluoric acid (aqueous, 48%), sulfuric acid (H₂SO₄, purity ≥ 95%), 1,3,5-benzenetricarboxylic acid (H₃BTC), selenic acid (aqueous, 40%) deuterated sulfuric acid (D₂SO₄, 96-98%, 99.5 atom % D) and D₂O (99.9 atom % D) was obtained from Aldrich. Deuterated 1,3,5-benzenetricarboxylic acid (D₃DBTC, 97%, 98 atom % D) was obtained from CDN Isotopes. Trimethylphosphine oxide (TMPO) was obtained from Alfa Aesar. Ammonium hydroxide (28%) was obtained from EMD Millipore. All starting materials and solvents, unless otherwise specified, were used without further purification.

Analytical techniques. Single-crystal x-ray diffraction (SXRD) data were collected on beamline 11.3.1 at the Advanced Light Source, Lawrence Berkeley National Lab. Samples were mounted on MiTeGen® kapton loops and placed in a 100(2) K nitrogen cold stream provided by an Oxford Cryostream 700 Plus low temperature apparatus on the goniometer head of a Bruker D8 diffractometer equipped with a PHOTON100 CMOS detector operating in shutterless mode. Diffraction data were collected using synchrotron radiation monochromated using a silicon (111) reflection to a wavelength of 0.7749(1) Å. An approximate full-sphere of data was collected using a combination of phi and omega scans with scan speeds of 2 seconds per 4 degrees for the phi fast scans, and 5 and 15 seconds per degree for the omega scans at $2\theta = 0$ and -45 , respectively. In all cases, the data were processed using the Bruker APEX2 software package (1, 2), structures were solved by intrinsic phasing (SHELXT) and refined by full-matrix least squares on F^2 (SHELXL-2014) using the Olex2 software package (3). All non-hydrogen atoms were refined anisotropically unless otherwise specified. Hydrogen atoms were geometrically calculated and refined as riding atoms. See Section 3 for more details.

Powder x-ray diffraction patterns (PXRD) were recorded using a Bruker D8 Advance diffractometer (Göbel-mirror monochromated Cu K_α radiation $\lambda = 1.54056$ Å). Elemental microanalyses (EA) for carbon, hydrogen, nitrogen and sulfur were performed in the Microanalytical Laboratory of the College of Chemistry at UC Berkeley, using a Perkin Elmer 2400 Series II CHNS elemental analyzer. Solution ¹H NMR spectra were acquired on a Bruker AVB-400 NMR spectrometer. N₂ sorption isotherms were measured on a Quantachrome Quadrasorb instrument, held at 77 K using a liquid nitrogen bath. Helium was used for the estimation of dead space for gas adsorption measurements. Ultra-high purity grade N₂ and He were used throughout the adsorption experiments.

Powder neutron diffraction data (PND) were collected at POWGEN at Oak Ridge National Laboratory, Tennessee. Two diffraction patterns were collected for each sample using center wavelengths 1.066 Å and 4.797 Å covering a d-spacing range of 0.5-15 Å.

Inductively coupled plasma-optical emission spectroscopy (ICP-OES) was performed on a PerkinElmer Optical Emission Spectrometer Optima 7000DV instrument. Scanning electron microscope (SEM) images were obtained using a Zeiss Gemini Ultra-55 analytical scanning electron microscope. FTIR spectra were collected in-house using a Bruker ALPHA Platinum ATR-FTIR Spectrometer equipped with a single reflection diamond ATR module.

General procedure for sample preparation. To reduce nucleation in the growth of MOF single-crystals, the inner surface of glass containers were rinsed with Sigmacote® siliconizing reagent, washed three times with acetone, and dried in oven before use. Following synthesis, the MOFs were washed with DMF. The molecular formulae of the MOFs were determined using a combination of elemental analysis (C, H, N and S), ¹H NMR (ratio of linker to formate) and ICP-OES (Zr, Se), and TGA-MS. A mixture of containing 20 μL of DMSO-*d*₆ and 580 μL of hydrofluoric acid (48 wt% in water) was used to digest 10 mg of each MOF for NMR measurements.

79 **Native MOF-808 synthesis.** Single crystals of MOF-808 was prepared following the reported
80 procedure (4). Briefly, $\text{ZrOCl}_2 \cdot 8\text{H}_2\text{O}$ (0.032 g, 0.10 mmol) and H_2BTC (0.022 g, 0.10 mmol) were
81 dissolved separately in 2 ml DMF, then both solutions were combined in a 20 ml scintillation vial and 4
82 ml formic acid was added. This mixture was then placed in a pre-heated oven at 100 °C for three days.
83 Colorless block crystals were collected in 81% yield based on Zr. As-synthesized MOF-808 single
84 crystals were immersed in anhydrous DMF for three days followed by water for three days, during which
85 time the solvent was exchanged three times per day. The same conditions were used for the preparation of
86 deuterated MOF-808, except deuterated D_2BTC was used as the starting reagent, and washing was
87 performed in D_2O instead of H_2O .

88 **Preparation of Sulfated MOF-808.** Approximately 50 mg of MOF-808 was immersed in 0.05
89 M sulfuric acid in H_2O for 24 hours and stirred at regular intervals. The treated solid was then washed
90 with H_2O , then solvent exchanged by immersion in anhydrous acetone before exchanging into chloroform.
91 For each step, the samples were washed for three days with the solvent being decanted and freshly
92 replenished three times per day. The chloroform in the solvent-exchanged crystals was removed under
93 dynamic vacuum (30 mTorr) for 24 h at room temperature, followed by 8 h at 80 °C and a further 16 h at
94 120 °C. The same conditions were used for the preparation of deuterated sulfated MOF-808, except
95 deuterated sulfuric acid in D_2O was used, and all aqueous washings were carried out with D_2O .

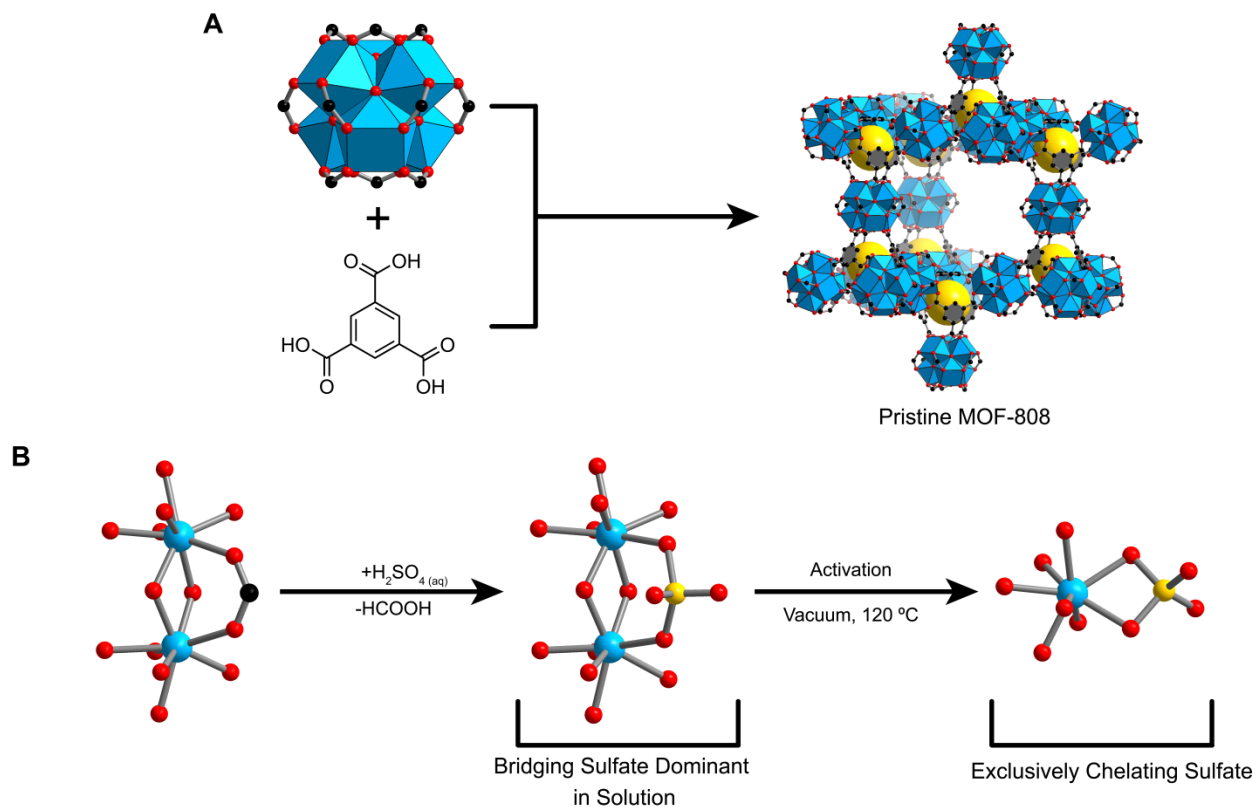
96 ^1H solution NMR spectra of the digested, activated and sulfated MOF-808 (400 MHz, DMSO-
97 d_6): 8.61 (s, BTC), 8.10 (s, HCOOH), 7.92 (s, DMF), peak area ratio (BTC:HCOOH:DMF) =
98 6.0:0.05:0.3. Anal calcd for $\text{Zr}_6\text{O}_4(\text{OH})_4(\text{C}_6\text{H}_3\text{O}_6)_2(\text{SO}_3)_{2.3}(\text{OH})_{1.4}(\text{OH}_2)_{3.1}(\text{C}_3\text{H}_7\text{NO})_{0.4} = \text{Zr}_6\text{O}_{34.1}\text{C}_{19.2}\text{H}_{20.4}\text{S}_{2.3}\text{N}_{0.4}$;
99 C = 16.2%; H, 1.4%; N, 0.4%; S, 5.2%. Found: C = 17.2%; H, 1.3%; N, 0.6%; S, 5.4%.

100 **Preparation of Selenated MOF-808.** Approximately 50 mg of MOF-808 was immersed in 0.05
101 M selenic acid in H_2O for 24 hours and stirred at regular intervals. The treated solid was then washed with
102 H_2O , then solvent exchanged by immersion in anhydrous acetone before exchanging into chloroform. For
103 each step, the samples were washed for three days with the solvent being decanted and freshly
104 replenished three times per day. The chloroform in the solvent-exchanged crystals was removed under
105 dynamic vacuum (30 mTorr) for 24 h at room temperature, followed by 8 h at 80 °C and a further 16 h at
106 120 °C.

107 ^1H solution NMR spectra of the digested, activated and selenated MOF-808 (400 MHz, DMSO-
108 d_6): 8.64 (s, BTC), 7.85 (s, DMF), peak area ratio (BTC:HCOOH:DMF) = 6.00:0.00:0.5. Calculated
109 formula $\text{Zr}_6\text{O}_4(\text{OH})_4(\text{C}_6\text{H}_3\text{O}_6)_2(\text{SeO}_4)_{2.3}(\text{OH})_{1.4}(\text{C}_3\text{H}_7\text{NO})_{0.5}(\text{H}_2\text{O})_{2.9} = \text{Zr}_6\text{O}_{34}\text{C}_{19.5}\text{H}_{20.7}\text{N}_{0.5}\text{Se}_{2.3}$; C, 15.3%; H, 1.4%; N,
110 0.5%. Found: C, 15.4%; H, 0.9%; N, 0.7%.

111 **Preparation of sulfated zirconia.** The synthesis of sulfated zirconia was performed following a
112 literature report of conventional sulfated zirconia with an additional step to prepare $\text{Zr}(\text{OH})_4$ from
113 $\text{ZrOCl}_2 \cdot 8\text{H}_2\text{O}$.(5) Briefly, 1g $\text{ZrOCl}_2 \cdot 8\text{H}_2\text{O}$ was placed in 10 mL NH_4OH (28%) and stirred overnight at
114 room temperature. The slurry was filtered and washed in deionized water before being dried at 50 °C. 1g
115 of the product, $\text{Zr}(\text{OH})_4$, was stirred for 2 h in 10 mL aqueous H_2SO_4 (0.05 M). The solid product was
116 subsequently filtered and dried at 100 °C for 24 h, followed by calcination at 550 °C for 2 h. The sulfur
117 loading was found to be 3.45%.

118



119

120 **Supplementary Figure 1. Synthesis and coordination mode of sulfate in MOF-808-SO₄.** (A) The
 121 synthesis of pristine MOF-808 constructed by 6-coordinate zirconium-based metal clusters containing
 122 formate groups and linked by benzenetricarboxylate into the diamond topology is depicted. Note that only
 123 five out of a possible six formates coordinate to the cluster, with water ligands replacing the last formate.
 124 These formates may be substituted with sulfate anions as in (B), which coordinate in a bidentate fashion
 125 to zirconium, predominantly by a bridging mode to two zirconium atoms when in solution, and convert to
 126 exclusively the chelating mode to a single zirconium atom following activation by heating under dynamic
 127 vacuum.

128 Section 2: Powder Neutron Diffraction Experiments

129 Approximately 300 mg activated pristine deuterated MOF-808 was packed into a 6 mm vanadium
 130 can sealed with a titanium collar, copper gasket and aluminum lid in an argon glove box. After post-
 131 synthetic exchange with 0.05 M D₂SO₄ in D₂O followed by activation described in Section 1, sulfated
 132 deuterated MOF-808 was similarly loaded into the vanadium can. In both cases, data was collected at 10
 133 K and 300 K for comparison.

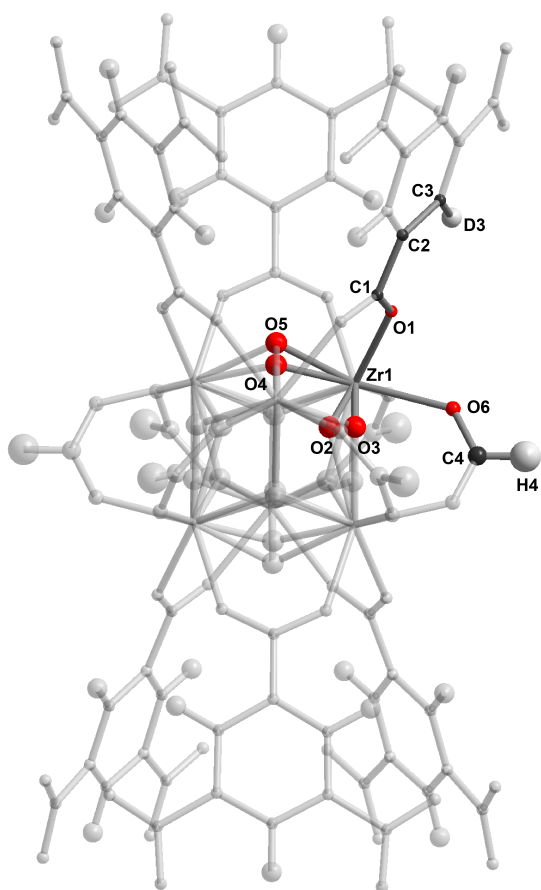
134
 135 Structure models were initially developed in Materials Studio 7.0 using the models from single
 136 crystal x-ray diffraction experiments as a starting point. These models were then refined against the
 137 powder neutron data, with atomic coordinates of the cluster and linker allowed to refine freely, with
 138 occupancies fixed based on the activated pristine MOF-808 model and knowledge of sulfate coordinates
 139 from the MOF-808-SO₄ sample prior to activation from single crystal and powder x-ray data.

140 Pristine MOF-808 modeling

141 An initial structural model was developed based on MOF-808 single crystal data collected prior
 142 to activation. All hydrogen atoms in the structure were converted to deuterium atoms except for hydrogen

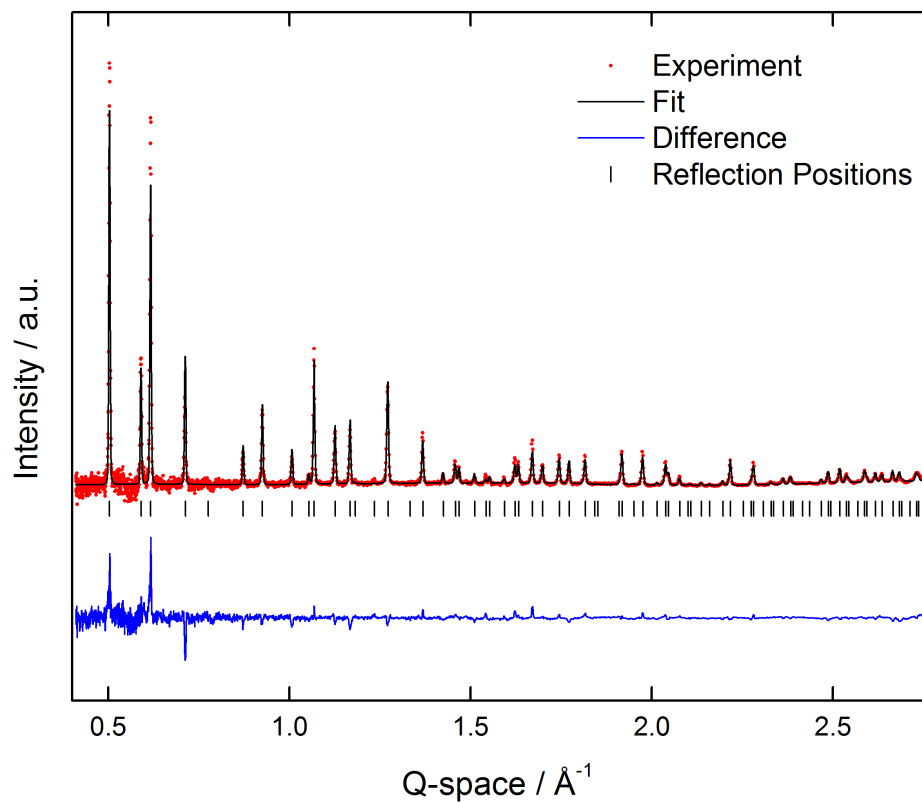
143 on formate, which was not deuterated. To begin with, atomic coordinates were allowed to refine freely
144 before being fixed at their converged values. With the linker and zirconium occupancies fixed at 100%,
145 the thermal ellipsoids and occupancies of the remaining atoms were systematically refined. Note that the
146 ellipsoids on the linker C1, C2, C3, and the ellipsoids of the μ -O and -OH pairs were constrained to be
147 identical in order to aid refinement. The occupancies of the μ -O and -OH groups O2, O3, O4 and O5
148 refined to 47.9 ± 1.0 , 48.7 ± 1.0 , $50.7 \pm 3.2\%$ and $49.5 \pm 3.2\%$ respectively, meaning there has been no
149 deprotonation of the μ -OH groups to account for charge-balancing. Note however that the data set
150 collected at room temperature failed to converge O5, and allowing the position of O4 to refine freely
151 moved it to intermediate coordinates between O4 and O5 in the data set collected at 10 K. This is not an
152 indication that O5 is not present as it is observed in the 10 K data set, but simply an averaging of the two
153 positions due to thermal motion.

154 The ellipsoids of D3A and D5, corresponding to μ -OD, failed to converge indicating only partial
155 exchange of hydrogen with deuterium. If hydrogen is partially present, this does not reflect the true
156 occupancy of deuterium at this position as ^1H and ^2D signals cancel each other out. This could be
157 additionally compounded from the terminal position of the deuterium atoms that increase disorder and
158 thermal motion as is observed for H4 on formate. The formate carbon and hydrogen atoms, C4 and H4,
159 refine to $84.1 \pm 1.1\%$ and $85.5 \pm 2.3\%$, fixed to 83.3% as consistent with NMR data. Refinement of O6,
160 which accommodated oxygen from formate and terminal water molecules coordinated zirconium,
161 converged at $97.9 \pm 0.8\%$, which is consistent with terminal hydroxide groups completing the charge-
162 balancing of the framework, and hence not being removed following activation as was found in MOF-
163 808-SO₄. The final refinement converged to $wR_p = 3.20\%$ and $R_p = 11.20\%$.



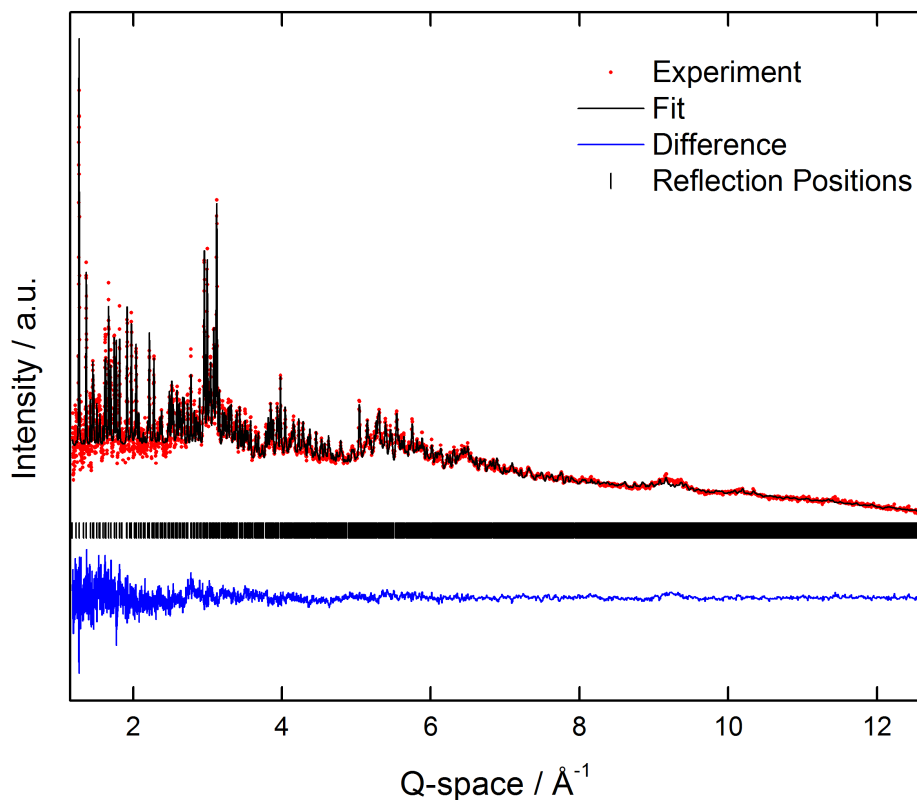
164

165 **Supplementary Figure 2.** Representation of metal oxide cluster in pristine MOF-808 as found by powder
166 neutron diffraction. The asymmetric unit is colored and labeled with zirconium in blue, oxygen in red,
167 carbon in black and hydrogen/deuterium in white, while the remaining atoms are shaded in order to show
168 how the framework extends. Thermal ellipsoids are represented at 50% probability, with all refined
169 isotropically. $wRp = 3.20\%$, $Rp = 11.20\%$



170

171 **Supplementary Figure 3.** Powder neutron diffraction pattern of data for pristine MOF-808 activated at
172 120 °C, displaying the experimental pattern (red) and the fitted pattern obtained by Rietveld refinement of
173 the structure (black). The difference plot (blue) as well as the Bragg positions (black) are provided.



174

175 **Supplementary Figure 4.** Powder neutron diffraction pattern of data collected at high Q-space values for
 176 pristine MOF-808 activated at 120 °C, displaying the experimental pattern (red) and the fitted pattern
 177 obtained by Rietveld refinement of the structure (black). The difference plot (blue) as well as the Bragg
 178 positions (black) are provided.

179

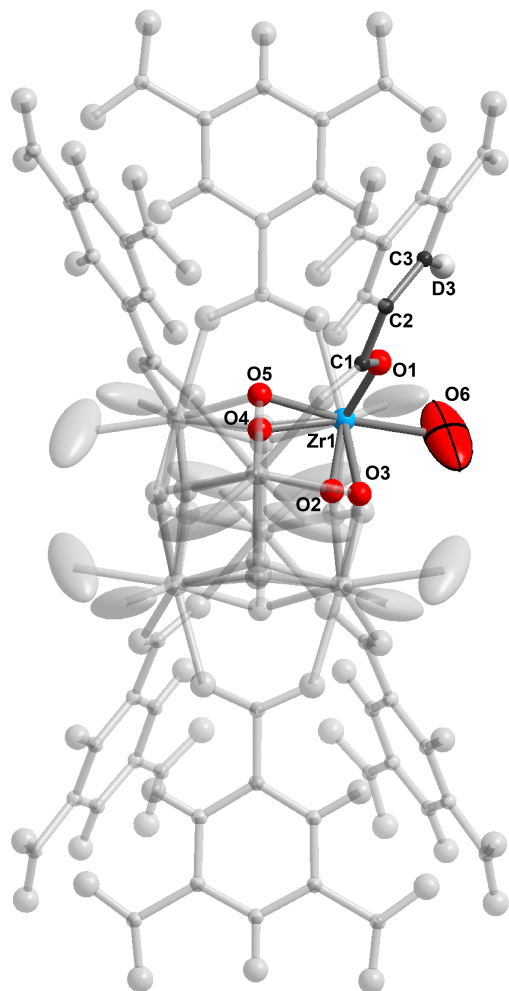
180 MOF-808-SO, modeling

181 The coordinates and occupancies from the sulfated MOF-808 model prior to activation were
 182 imported and used as a starting point for Rietveld refinement. To begin with, atomic coordinates were
 183 allowed to refine freely before being fixed at their converged values. With the linker and zirconium
 184 occupancies fixed at 100%, the thermal ellipsoids and occupancies of the remaining atoms were
 185 systematically refined. Note that the ellipsoids on the linker C1, C2, C3, and the ellipsoids of the μ -O and
 186 -OH pairs were constrained to be identical in order to aid refinement. It was found that modeling S1, S2,
 187 O8A, O8B, O9A and O9B based on coordinates from single crystal data failed to converge with
 188 reasonable thermal ellipsoids. This is due to the very low occupancies of sulfate, found to be 12% and 6%
 189 for S1 and S2 in MOF-808-SO, respectively, and prior to activation. It should be noted that the coherent
 190 neutron scattering length for sulfur is less than half that of oxygen, in contrast with x-ray diffraction
 191 where sulfur contains double the number of electrons as oxygen and thus scatters x-rays much more
 192 readily. Since the refinement quality indicators, wR_r and R_p , displayed no significant difference between
 193 modeling and neglecting the sulfate groups, and requiring significant restraints to model whilst worsening
 194 the overall refinement quality, all sulfate atoms except for O6, which is oxygen bound to zirconium
 195 directly, were neglected in the final structure model. The presence of sulfate in the activated structure was
 196 however confirmed by elemental analysis and lack of formate by ^1H NMR, and evidence for the sulfate

197 position in the framework was identified through PXRD as being exclusively in the chelating mode (see
198 Section 4).

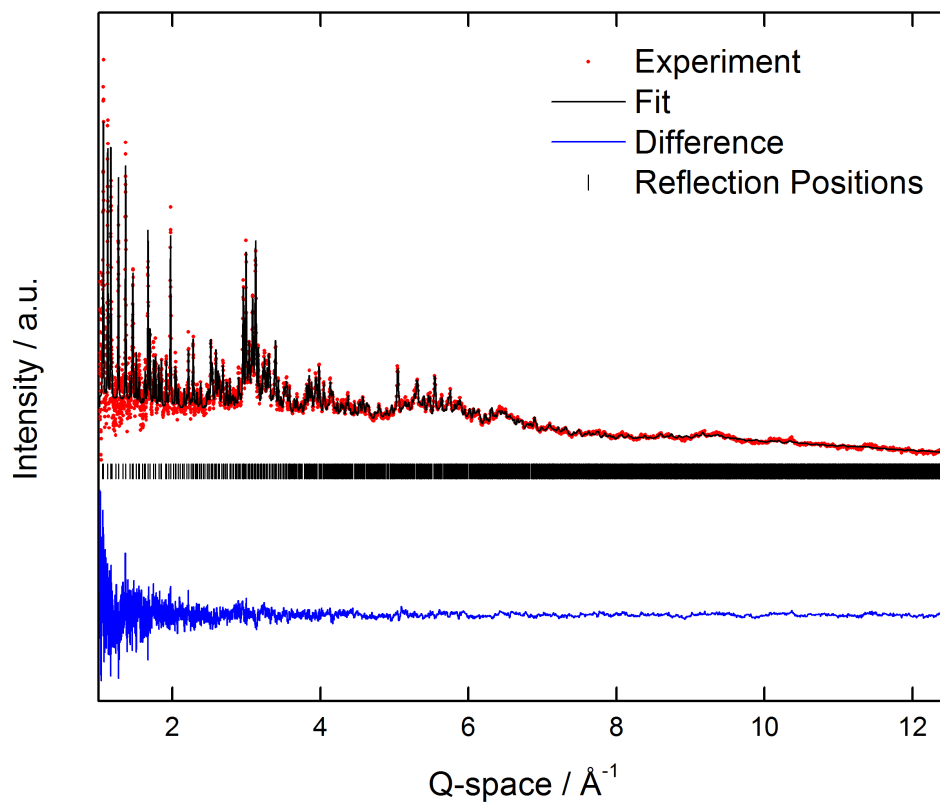
199 Additionally, it was found that the thermal ellipsoid of D3A and D5, corresponding to deuterium
200 on μ -OD in the framework, failed to converge. This could be evidence for deprotonated μ -OD in the
201 framework; however, free refinement of the occupancies of the corresponding oxygen atoms on the μ -O
202 and -OD groups, O2 ($53.5 \pm 1.1\%$) and O3 ($48.5 \pm 1.1\%$) for D3 and O4 ($49.8 \pm 2.1\%$), O5 (50.8 ± 2.1) for
203 D5 were found to be, within two standard deviations, in an equal ratio as in the sample prior to activation.
204 It is therefore presumed not all deuterium was successfully exchanged into the framework, since any
205 hydrogen present in the same position has a negative scattering length and would negate the signal from
206 deuterium. Indeed, a roughly 1:2 ratio of D to H would contribute overall no scattering. This could be
207 additionally compounded from the terminal position of the deuterium atoms that increase disorder and
208 thermal motion.

209 At position O6, where sulfate and water coordinate to zirconium in the sample prior to activation,
210 the occupancy refines to $78.7 \pm 1.1\%$, yet the contribution from sulfate only accounts for 38.3%, or 4.6
211 oxygen atoms out of 12 possible sites per cluster. Since the remaining density must be derived from
212 water, and having established charge-balancing is not achieved elsewhere, we postulate some of this
213 density must be deprotonated water to become terminal hydroxide. Based on the chemical formula, there
214 is an average charge of -1.4 per cluster unaccounted for, and therefore 11.7% of this density is assigned to
215 hydroxide, or 1.4 out of the 12 possible positions per cluster, (two per zirconium). In total, sulfate and
216 hydroxide account for 50% of the observed density, leaving $28.7 \pm 1.1\%$ as water molecules bound to the
217 zirconium cluster, which translates to 3.4 ± 0.1 water molecules per cluster, and the remaining $21.6 \pm 1.1\%$
218 unoccupied positions corresponding to open metal sites. This result is consistent with previous
219 experimental data indicating Lewis acid sites alongside Brønsted acid sites in MOF-808-SO₄ (4). While
220 the thermal ellipsoid for O6A is relatively large compared to other atoms in the structure, with at least
221 three different species in different local environments and slightly different positions for each, this is
222 reasonable. In the sample prior to activation with single crystal data, a larger anisotropic ellipsoid is also
223 observed at position O6, reflecting the slightly strained conformation of the two binding modes of sulfate,
224 which are not perfectly overlapping with the oxygen atom from coordinated water, which illustrates this
225 point.



226

227 **Supplementary Figure 5.** Representation of metal oxide cluster in MOF-808-SO₄ as found by powder
 228 neutron diffraction. The asymmetric unit is colored and labeled with zirconium in blue, oxygen in red,
 229 carbon in black and deuterium in white, while the remaining atoms are shaded in order to show how the
 230 framework extends. Note the large ellipsoid for O6 relative to other atoms is expected as this position is
 231 representing at least four different sources of oxygen atoms including from water, hydroxide, bridging
 232 and chelating sulfate. Thermal ellipsoids are represented at 50% probability, with all except O6 refined
 233 isotropically. wRp = 2.91%, Rp = 9.59%



234

235 **Supplementary Figure 6.** Powder neutron diffraction pattern of data collected at high Q-space values for
236 MOF-808-SO₄ activated at 120 °C, displaying the experimental pattern (red) and the fitted pattern
237 obtained by Rietveld refinement of the structure (black). The difference plot (blue) as well as the Bragg
238 positions (black) are provided.

239

240 **Section 3: Single Crystal X-ray Diffraction Analyses**

241

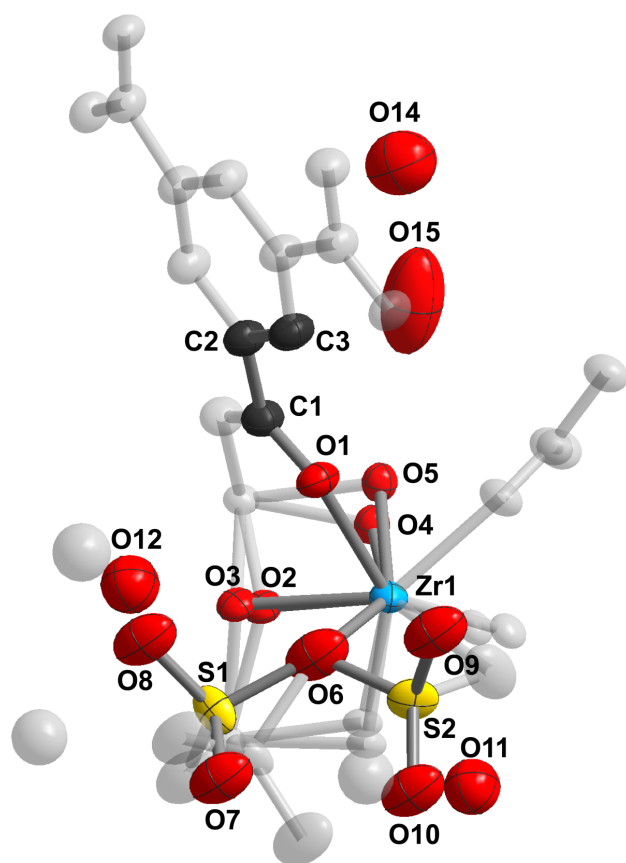
242 **Supplementary Table 1.** Crystal structure data for pristine MOF-808 prior to activation.

243

Sample	Pristine MOF-808
chemical formula	Zr ₆ O _{7.12} C ₂₃ H ₁₅
formula mass	1432.67
crystal system	cubic
space group	<i>Fd-3m</i>
λ (Å)	0.77490
a (Å)	35.1364(13)
Z	16
V (Å³)	43378(5)
temperature (K)	100
size /mm	0.015 × 0.015 × 0.010
density (g/cm³)	0.877
measured reflections	60241
unique reflections	2487
parameters	78
restraints	0
R_m	0.0858
θ range (deg)	2.10-30.74
R_i, wR_i	0.0531, 0.1907
S (GOF)	1.110
max/min res. dens. (e/Å³)	0.75/-0.89

244

Sample	MOF-808-SO ₄
chemical formula	Zr ₆ O _{43.09} C ₁₈ H ₁₀ S _{1.79}
formula mass	1520.35
crystal system	cubic
space group	<i>Fd-3m</i>
λ (Å)	0.77490
a (Å)	35.2075(13)
Z	16
V (Å ³)	43642(5)
temperature (K)	100
size /mm	0.015 × 0.015 × 0.010
density (g/cm ³)	0.926
measured reflections	70715
unique reflections	3175
parameters	101
restraints	7
R _{int}	0.0849
θ range (deg)	2.09-33.75
R ₁ , wR ₂	0.0556, 0.1911
S (GOF)	1.117
max/min res. dens. (e/Å ³)	1.1/-0.6

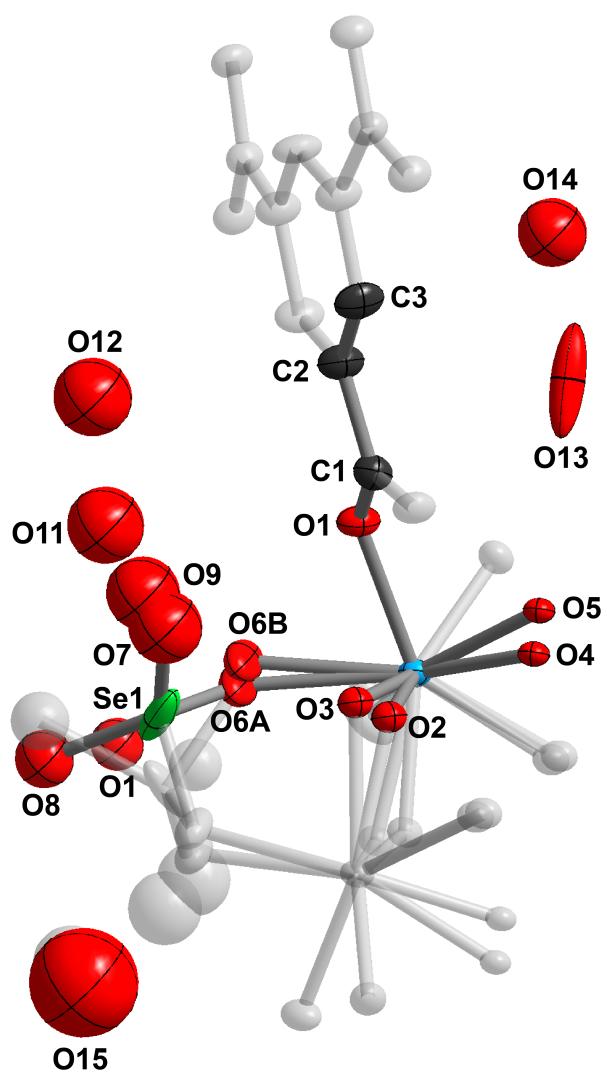


267
 268 **Supplementary Figure 8.** Representation of MOF-808-SO₄ prior to activation from SXR data. The
 269 asymmetric unit is displayed in color, with additional atoms in gray to aid visualizing the structure.
 270 Thermal ellipsoids are displayed at 50% probability and atom colors are as follows: zirconium (blue),
 271 oxygen (red), carbon (black), sulfur (yellow). Hydrogen atoms are omitted for clarity.

272
 273 The single crystal structure of MOF-808-SeO₄ was modeled where the occupancy of sulfur was
 274 permitted to refine freely, with Se1 exclusively existing in the bridging mode in the pre-activated form.
 275 Note this configuration changes to exclusively chelating upon activation under dynamic vacuum at 120
 276 °C. Ellipsoids of O2 and O3, O4 and O5, O6A and O6B were constrained in their pairs to be identical due
 277 to their close proximity. Oxygen atoms have been modeled within the cavity of the structure, representing
 278 highly disordered solvent molecules which are typically hydrogen bonding to the framework and are
 279 likely a combination of water and DMF molecules. Note that O7 through to O15 have been modeled
 280 isotropically due to their low occupancy and proximity to other atoms in the model. The geometry of
 281 selenate was restrained to its known tetrahedral configuration using distance and angle restraints due to
 282 partial occupancy and positional overlap with solvent molecules. Two low-angle reflections, (222) and
 283 (044), were omitted from the refinement due to their large discrepancy between calculated and
 284 experimental values. The reason for discrepancy is likely related to not fully accounting for the highly
 285 disordered solvent within the cavity.

286
 287 **Supplementary Table 3.** Crystal structure data for MOF-808-SeO₄ prior to activation.

Sample	MOF-808-SeO ₄
chemical formula	Zr ₆ O _{43.90} C ₁₈ H ₁₀ Se _{1.28}
formula mass	1579.22
crystal system	cubic
space group	<i>Fd-3m</i>
λ (Å)	0.77490
a (Å)	35.2645(10)
Z	16
V (Å ³)	43854(4)
temperature (K)	100
size /mm	0.015 × 0.015 × 0.010
density (g/cm ³)	0.955
measured reflections	79733
unique reflections	2245
parameters	98
restraints	17
R _{int}	0.0858
θ range (deg)	1.8-29.5
R ₁ , wR ₂	0.0510, 0.1672
S (GOF)	1.144
max/min res. dens. (e/Å ³)	0.8/-0.4



289

290 **Supplementary Figure 9.** Representation of MOF-808-SeO, prior to activation from SXRD data. The
 291 asymmetric unit is displayed in color, with additional atoms in gray to aid visualizing the structure.
 292 Thermal ellipsoids are displayed at 50% probability and atom colors are as follows: zirconium (blue),
 293 oxygen (red), carbon (black), selenium (green). Hydrogen atoms are omitted for clarity.

294

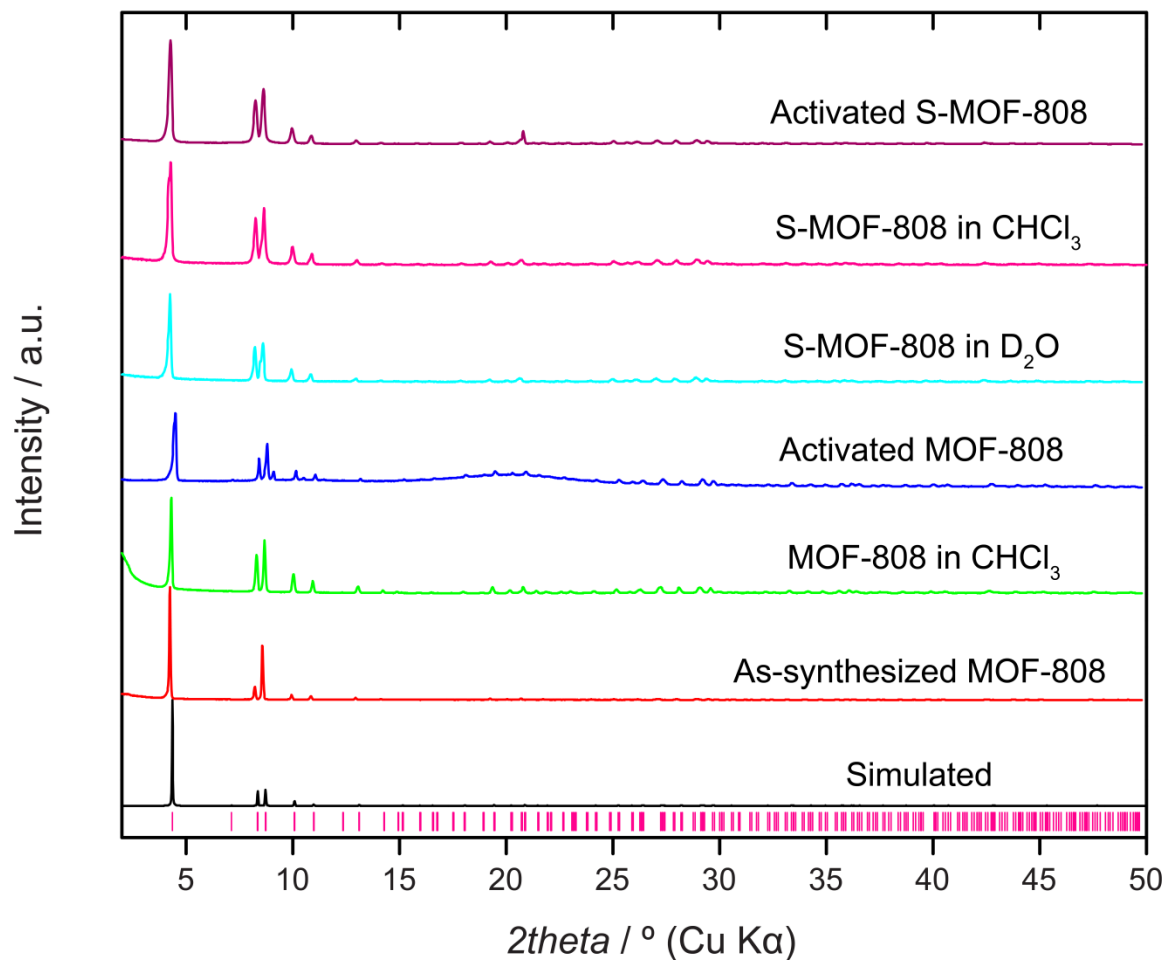
295

296

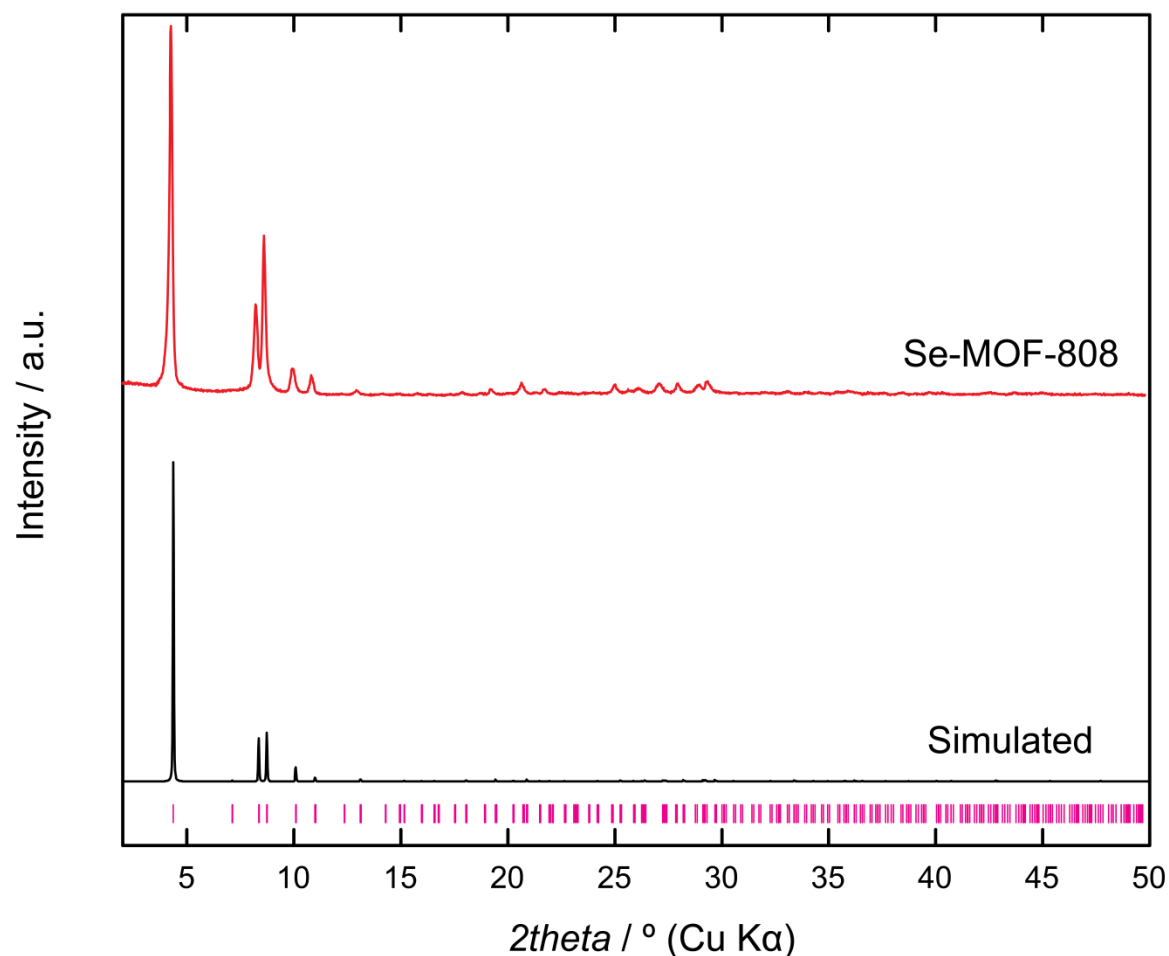
297

298

299



302
303 **Supplementary Figure 10.** PXRD patterns of deuterated MOF-808 after various stages of treatment. The
304 pristine simulated pattern (black) is compared to the as-synthesized (red), after CHCl₃ (green), and after
305 activation under dynamic vacuum (dark blue) of the pristine sample. The remaining patterns are
306 immediately after treatment with D₂SO₄ in D₂O (light blue), exchanging with CHCl₃ (pink) and activation
307 of the sulfated sample (violet), showing crystallinity is retained.



309

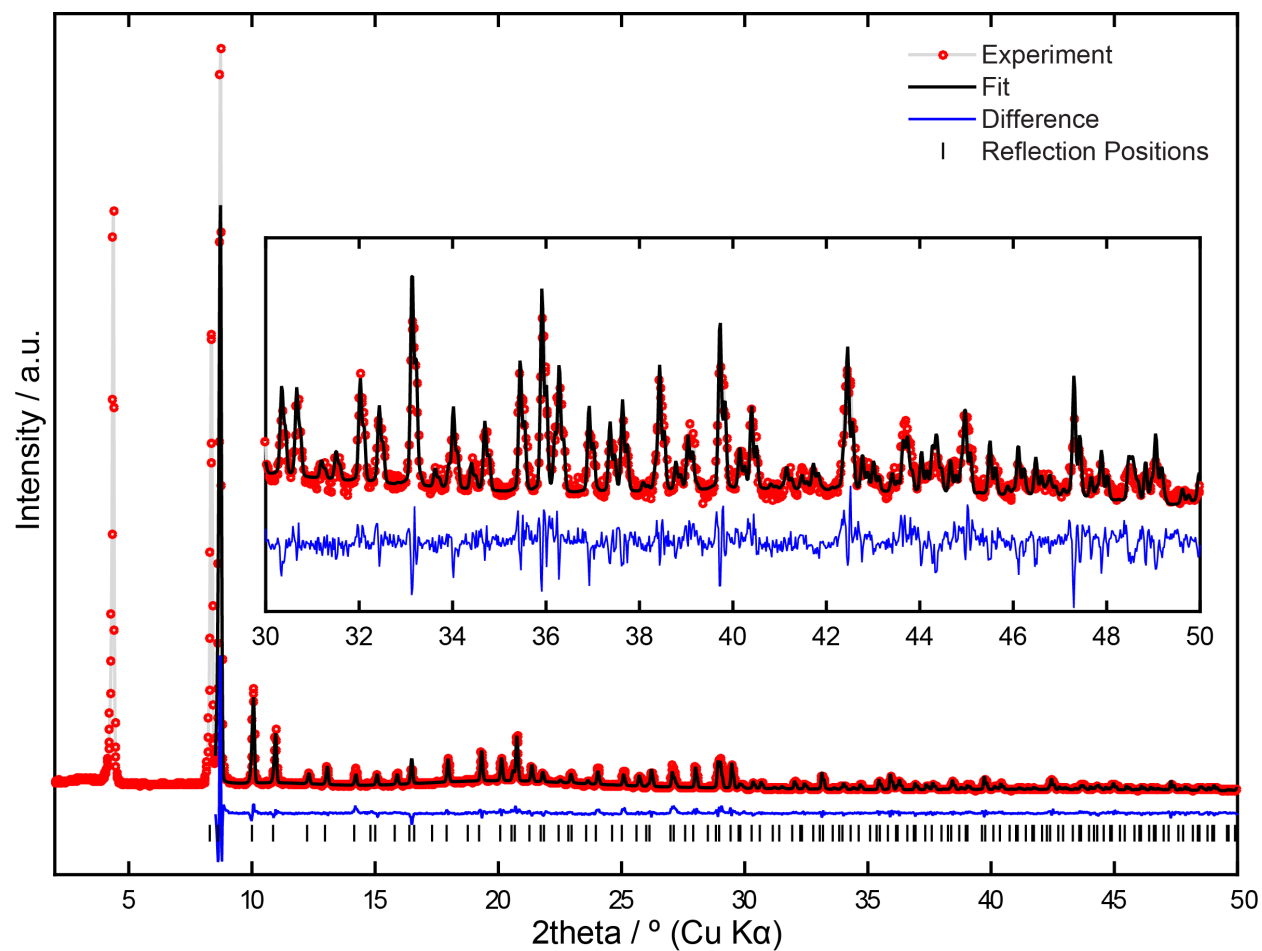
310 **Supplementary Figure 11.** PXRD patterns of simulated MOF-808 (black) and after immersion with 0.05
 311 M of selenic acid, solvent exchange and activation (red).

312 X-ray powder Rietveld refinements of the activated samples under argon (both MOF-
 313 808-SeO₄ and MOF-808-SO₄) were carried out using TOPAS 5 (6). Regarding the overall quality
 314 of the fits, it is noted that there is no routine like Platon SQUEEZE used, which could take the
 315 contribution of any residual density in the pores into account, such as the disordered argon atoms
 316 or any other remaining molecules. Thus, there are small systematic deviations visible in the
 317 difference plots, which might be due to anything what is left in the pores. Also, reflections 111
 318 and 022 had to be excluded from the refinements, as the inclusion of those two reflections
 319 rendered the refinement unstable and yielded chemically unreasonable electron densities in the
 320 $F_{\text{obs}}-F_{\text{calc}}$ plots. This data was used to determine the position of selenate and sulfate only, and the
 321 neutron data collected from the spallation source was used for occupancies and thermal ellipsoid
 322 parameters discussed in the main text due to the superior data quality and resolution obtained.

323

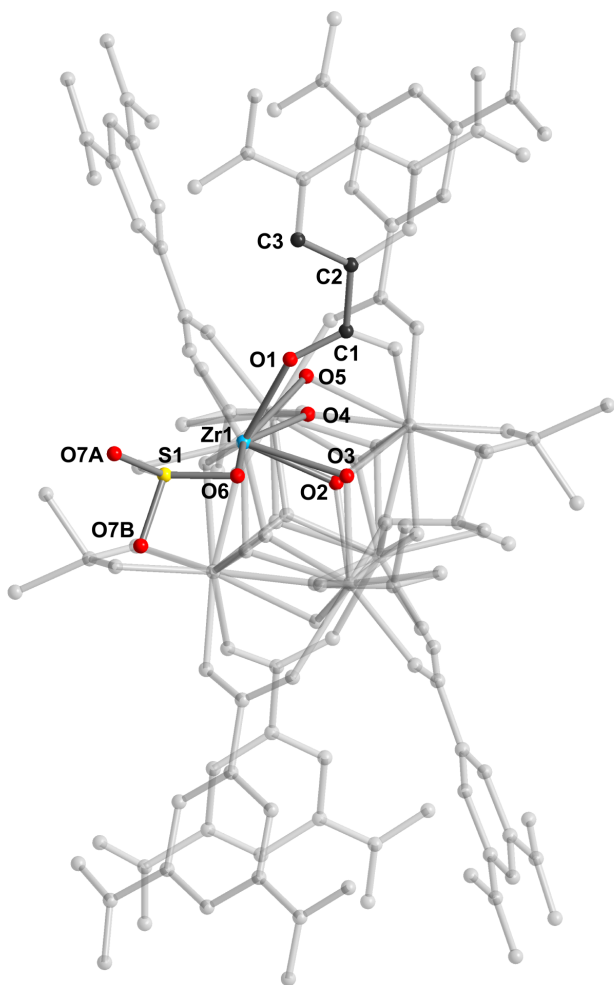
324 In the first steps of the refinement, a structure model was used without selenate/sulfate
 325 groups. In subsequent steps, those groups were located after inspection of the $F_{\text{obs}}-F_{\text{calc}}$ plots.
 326 Geometrical constraints were applied during the refinement to retain symmetry $Fd\bar{3}m$: In

327 particular, the Zr₆-octahedra were allowed to expand/contract isotropically. The phenyl ring of
328 the BTC linker was allowed to move along the 3-fold axis. The angle between the center of the
329 phenyl ring, the carbon atom the carboxylate group is binding to and the carboxylate carbon,
330 however, were refined freely, as a slight distortion of the linker was observed in previous work
331 (4). Interatomic distances within the linker were constrained to their ideal values. Further
332 constraints were applied to all oxygen atoms bound to the cluster and the selenate/sulfate as well
333 as S/Se atoms themselves, to ensure they stayed on their ideal Wyckoff position. Anti-bump
334 restraints were applied to the terminal oxygen atoms bound to S/Se. As of the low x-ray
335 scattering contrast of hydrogen, no hydrogen atoms were refined other than the ones directly
336 bound to the linker. In total, 3 isotropic displacement parameters were refined for the Se data.
337 Specifically, one displacement parameter for the zirconium atom, one for all light elements
338 besides the oxygens bridging zirconium and Se, and one for the selenate group. The results are as
339 expected: $U_{\text{iso}}(\text{Zr}) < U_{\text{iso}}(\text{light atoms}) < U_{\text{iso}}(\text{selenate})$. The occupancy of the selenate/sulfate group
340 was allowed to refine freely and is within the limits of the method and in reasonable agreement
341 with the results from ICP and EA respectively. It has to be noted that the fit is worse for the S
342 data than for Se. A reason for this could be the lower resolution. As a consequence, less
343 parameters were refined. In particular the displacement parameters were fixed at reasonable
344 values (0.03 for Zr, 0.05 for light atoms and 0.08 for the sulfate group). The chelating position of
345 the sulfate group however was verified by inspecting the $F_{\text{obs}} - F_{\text{calc}}$ plots. No significant electron
346 density was found at a hypothetical bridging position.



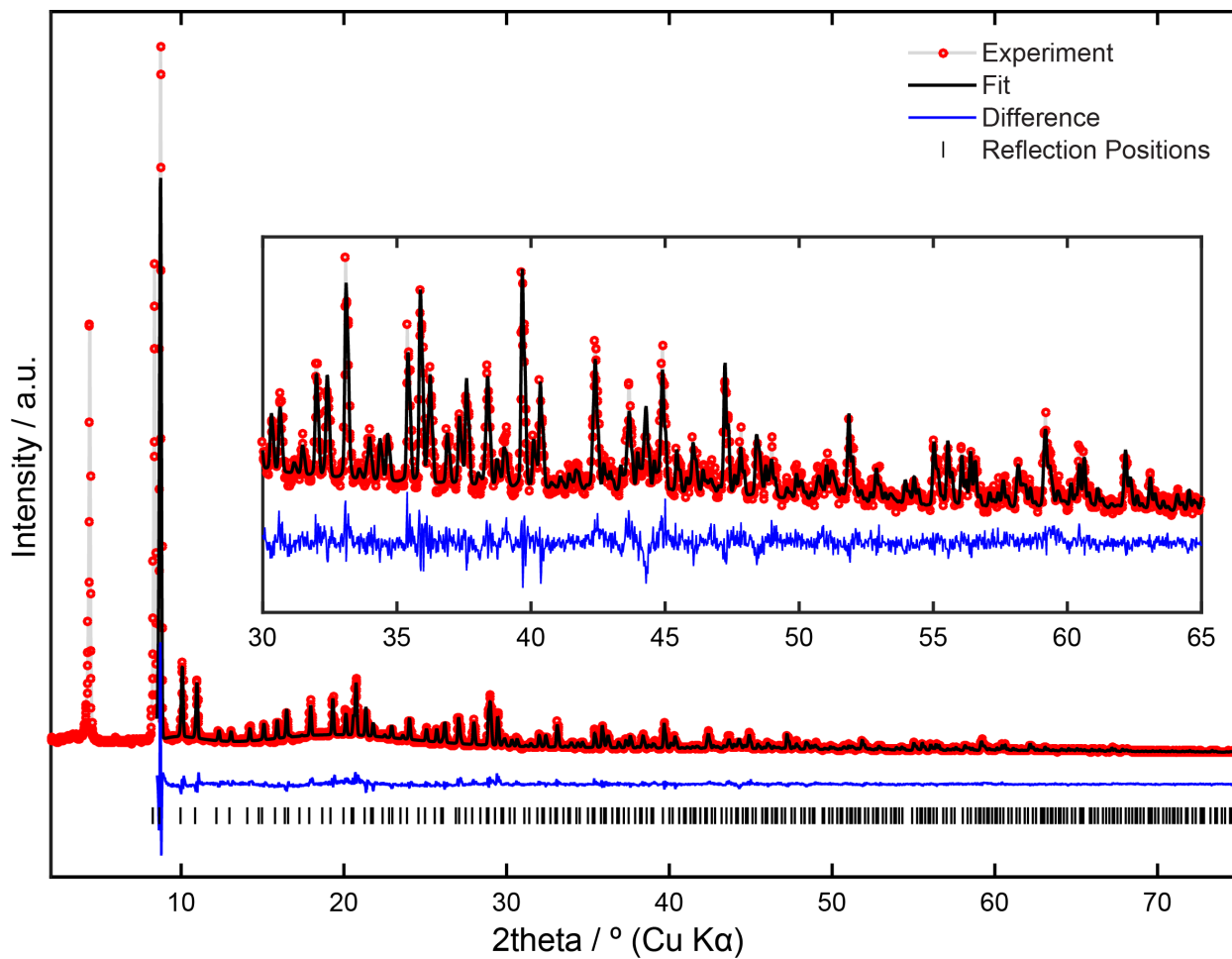
347

348 **Supplementary Figure 12.** Powder x-ray diffraction pattern of MOF-808-SO₄ activated at 120 °C,
349 displaying the experimental pattern (red) and the fitted pattern obtained by Rietveld refinement of the
350 structure (black). The difference plot (blue) as well as the Bragg positions (black) are provided. The data
351 was collected under argon atmosphere at room temperature.



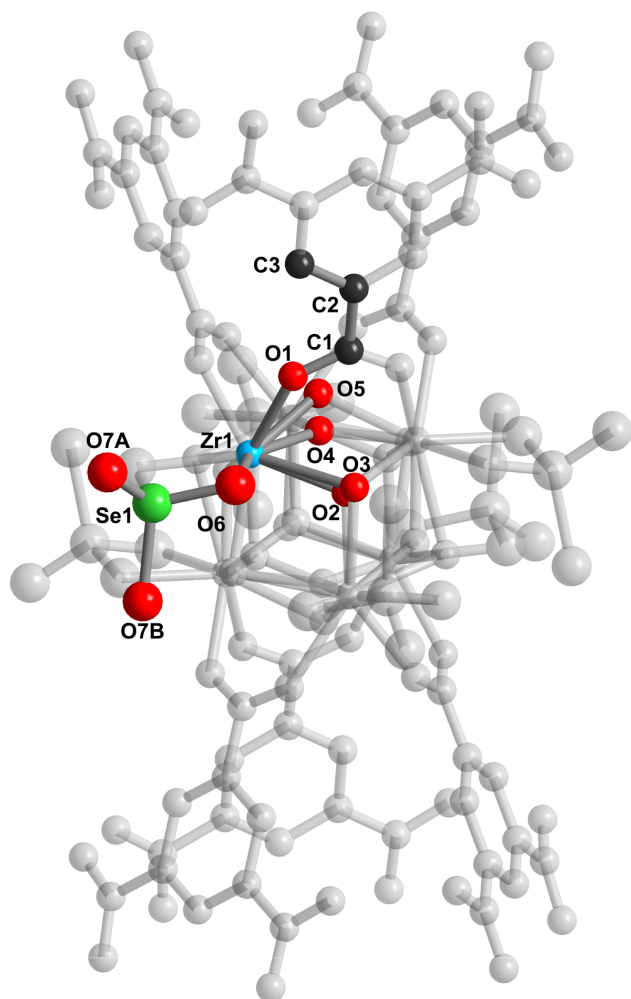
352

353 **Supplementary Figure 1.** Representation of metal oxide cluster in MOF-808-SO₄ as found by powder x-
354 ray diffraction, revealing the exclusively chelating mode of sulfate. The asymmetric unit is colored and
355 labeled with zirconium in blue, oxygen in red, carbon in black and sulfur in yellow, while the remaining
356 atoms are shaded in order to show how the framework extends. Hydrogen atoms were omitted for clarity.
357 Thermal ellipsoids are represented at 50% probability, with all refined isotropically. Rp = 11.6%.



358

359 **Supplementary Figure 2.** Powder x-ray diffraction pattern of MOF-808-SeO₂, activated at 120 °C,
 360 displaying the experimental pattern (red) and the fitted pattern obtained by Rietveld refinement of the
 361 structure (black). The difference plot (blue) as well as the Bragg positions (black) are provided. The data
 362 was collected under argon atmosphere at room temperature.



363

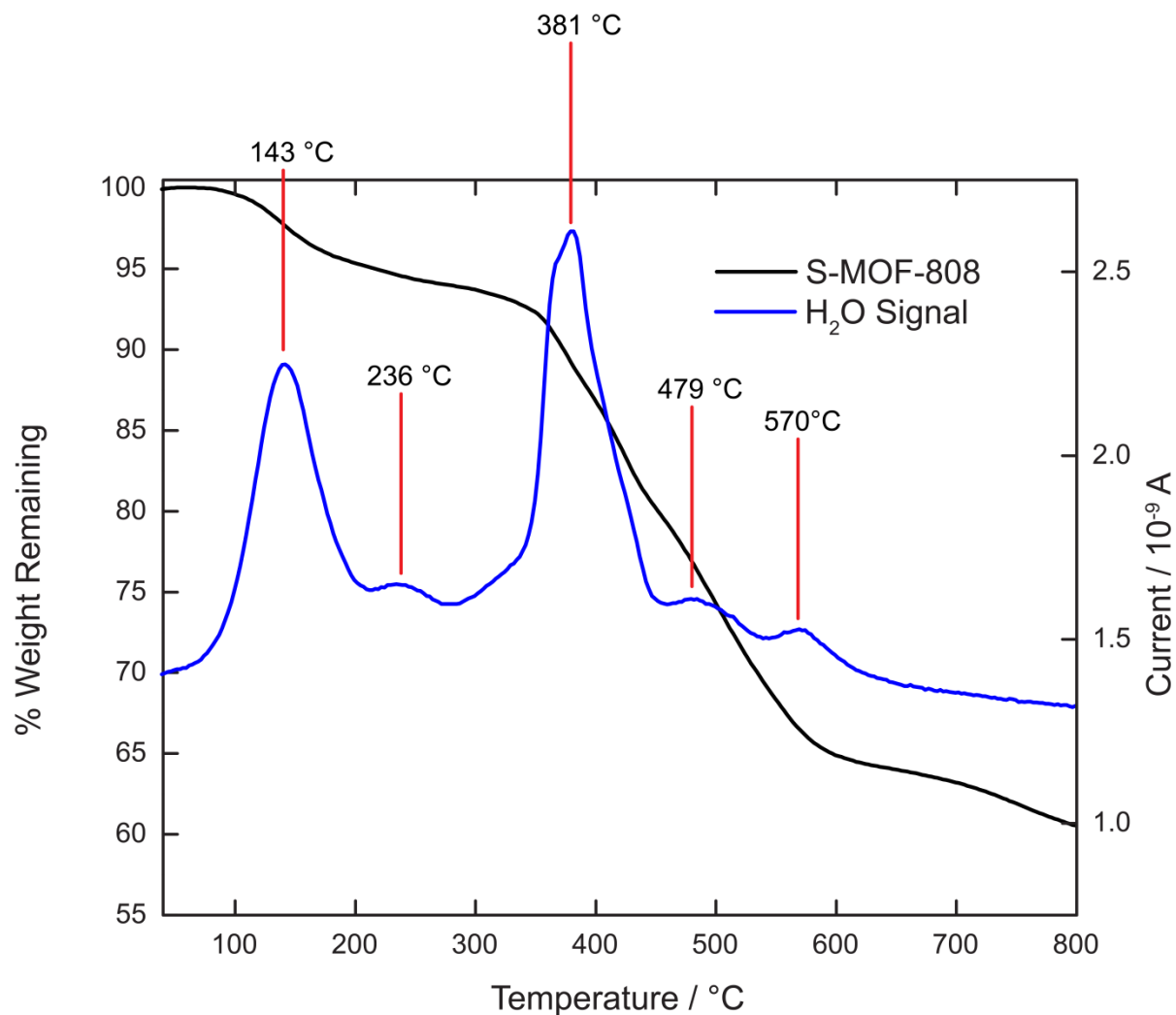
364 **Supplementary Figure 3.** Representation of metal oxide cluster in MOF-808-SeO, as found by powder x-
365 ray diffraction, revealing the exclusively chelating mode of selenate. The asymmetric unit is colored and
366 labeled with zirconium in blue, oxygen in red, carbon in black and sulfur in yellow, while the remaining
367 atoms are shaded in order to show how the framework extends. Hydrogen atoms were omitted for clarity.
368 Thermal ellipsoids are represented at 50% probability, with all refined isotropically. $R_p = 10.5\%$.

369

370 Section 5: Thermogravimetric Analysis

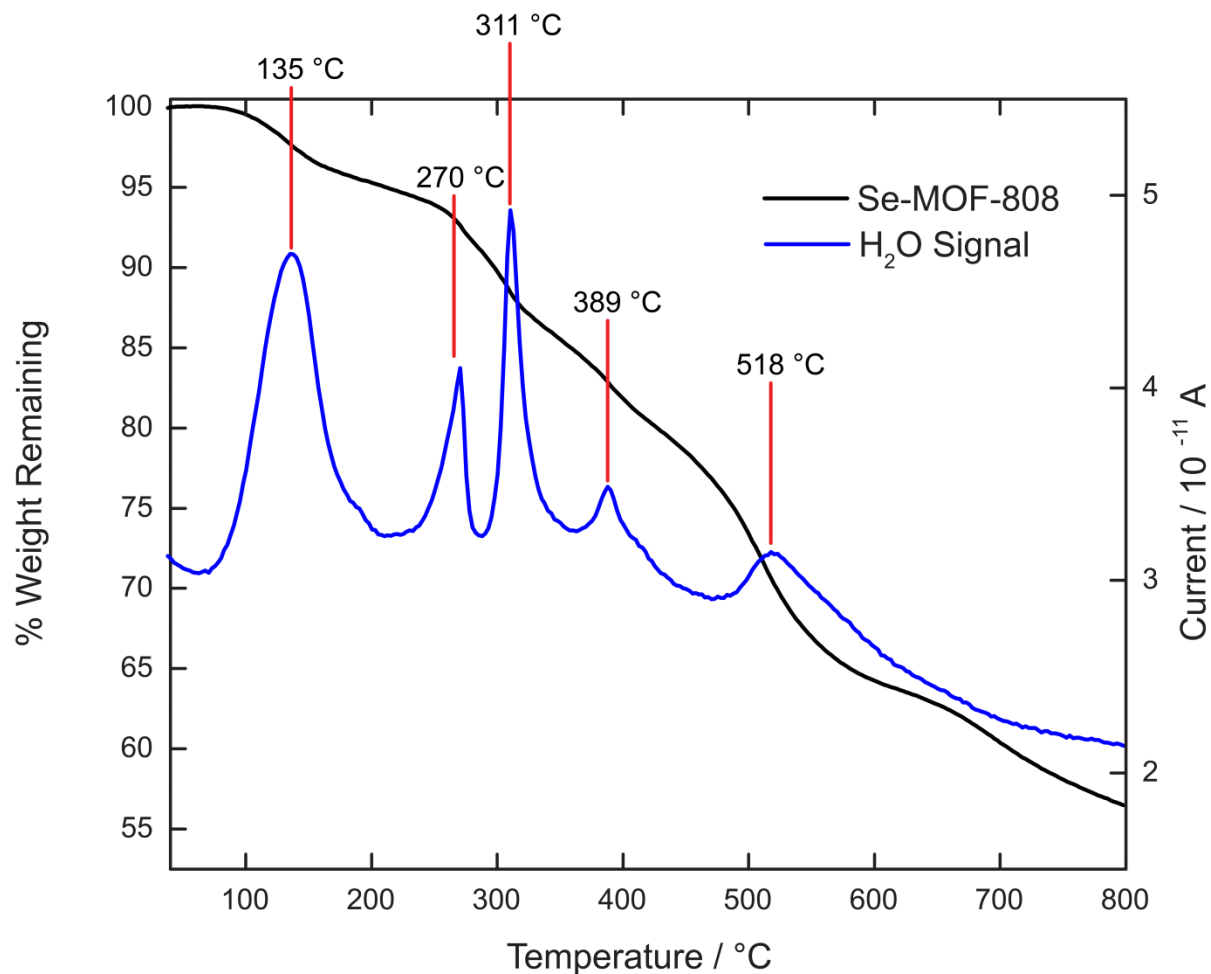
371

372 Thermogravimetric analysis coupled to a mass spectrometer (TGA-MS) was performed
373 using a Netzsch STA 449 F5 Jupiter thermogravimetric analyzer coupled to a Netzsch QMS 403
374 D Aeolos mass spectrometer. A typical sample preparation method is as follows: the activated
375 MOF sample was weighed in a glove box under argon atmosphere and transferred under argon to
376 the TGA-MS. The sample chamber was then evacuated three times, refilling the chamber each
377 time with argon. Next, the sample was heated at a rate of 2 °C min⁻¹ to 800 °C with an argon flow
378 rate of 20 ml min⁻¹. The water signal was quantified by repeating the experiment under identical
379 conditions but with copper sulfate pentahydrate as a standard since this compound has well-
380 characterized water loss steps. The area underneath the water signal plot was then used to
381 quantify the amount of water being lost in the MOF by relating this to the known amount lost in
382 the standard. The first water signal, peaking at 143 °C, corresponds to 0.96 mg H₂O in 24.5 mg
383 MOF-808-SO₄, which is 3.9% of the total mass. Taking the chemical formula of
384 $Zr_6O_4(OH)_4(C_9H_3O_6)_2(SO_4)_{2.3}(OH)_{1.4}(OH_2)_x(DMF)_{0.4} = Zr_6O_{31+x}C_{19.2}H_{14.2+2x}S_{2.3}N_{0.4}$, and assuming all terminal
385 water molecules are lost after the first peak, then $x = 3.1$. This result is consistent with the PND
386 data which indicates 3.4 ± 0.1 water molecules per cluster. A similar calculation was performed
387 on MOF-808-SeO₄, containing 3.4% H₂O by weight. Considering the formula
388 $Zr_6O_4(OH)_4(C_9H_3O_6)_2(SeO_4)_{2.3}(OH)_{1.4}(C_2H_7NO)_{0.5}(H_2O)_1 = Zr_6O_{31.1}C_{19.5}H_{14.5}N_{0.5}Se_{2.3} + xH_2O$, then $x = 2.9$.



389

390 **Supplementary Figure 4.** TGA-MS plot of activated MOF-808-SO₄ under argon atmosphere with the
 391 thermogravimetric plot (black) and corresponding water loss signal (blue). The first mass loss, with the
 392 water signal peaking at 143 °C, corresponds of water coordinated to the framework that is lost prior to full
 393 structure decomposition beginning around 320 °C. Quantification of the water signals correspond to 3.1
 394 water molecules per cluster for the first peak centered at 143 °C, 0.05 water molecules per cluster at 236
 395 °C, and 4.5 water molecules at 381 °C.



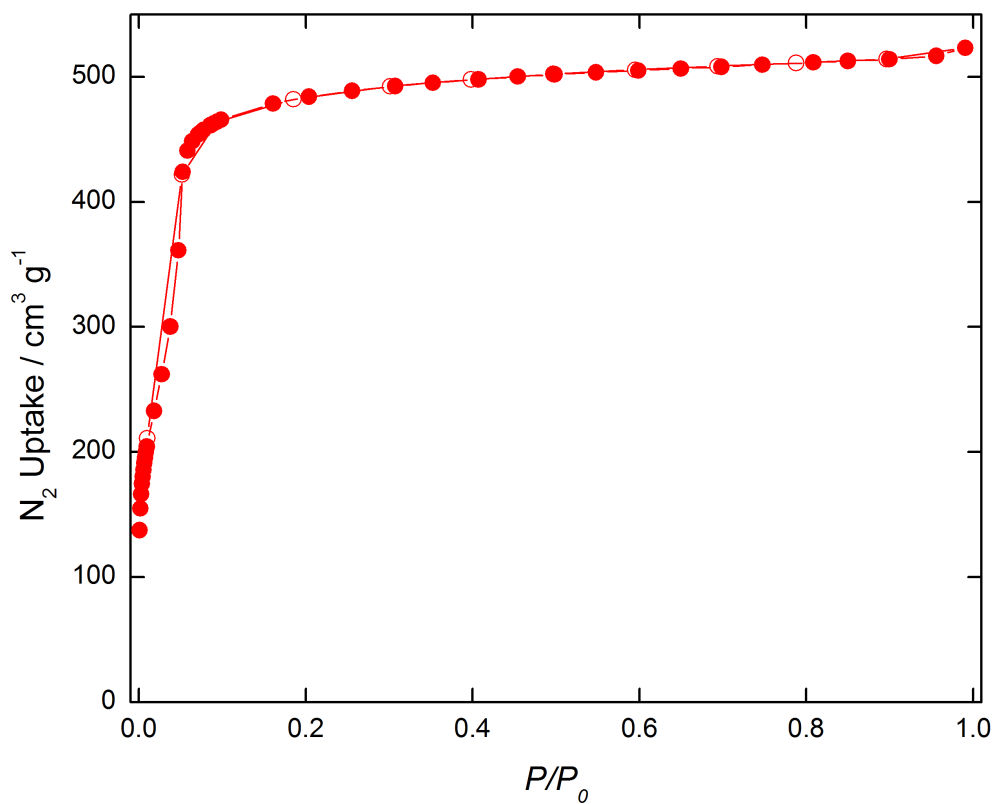
396

397 **Supplementary Figure 5.** TGA-MS plot of activated MOF-808-SeO₄ under argon atmosphere with the
 398 thermogravimetric plot (black) and corresponding water loss signal (blue). The first mass loss, with the
 399 water signal peaking at 135 °C, corresponds to water coordinated to the framework that is lost prior to full
 400 structure decomposition beginning around 270 °C. The most credible explanation for the lower
 401 temperature decomposition of MOF-808-SeO₄ compared to MOF-808-SO₄ is the much larger strain on
 402 chelating selenate, since the former is distorted to a much greater degree compared with chelating sulfate.
 403 Quantification of the water signals correspond to 2.9 water molecules per cluster for the first peak
 404 centered at 135 °C.

405

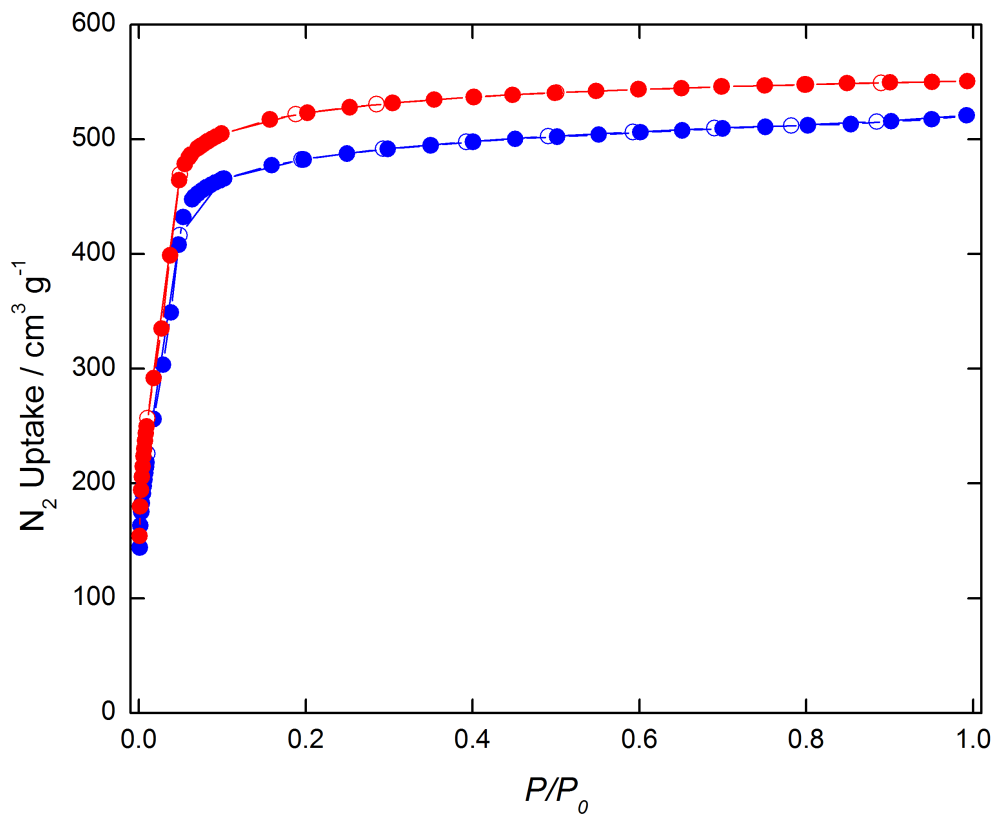
406

407

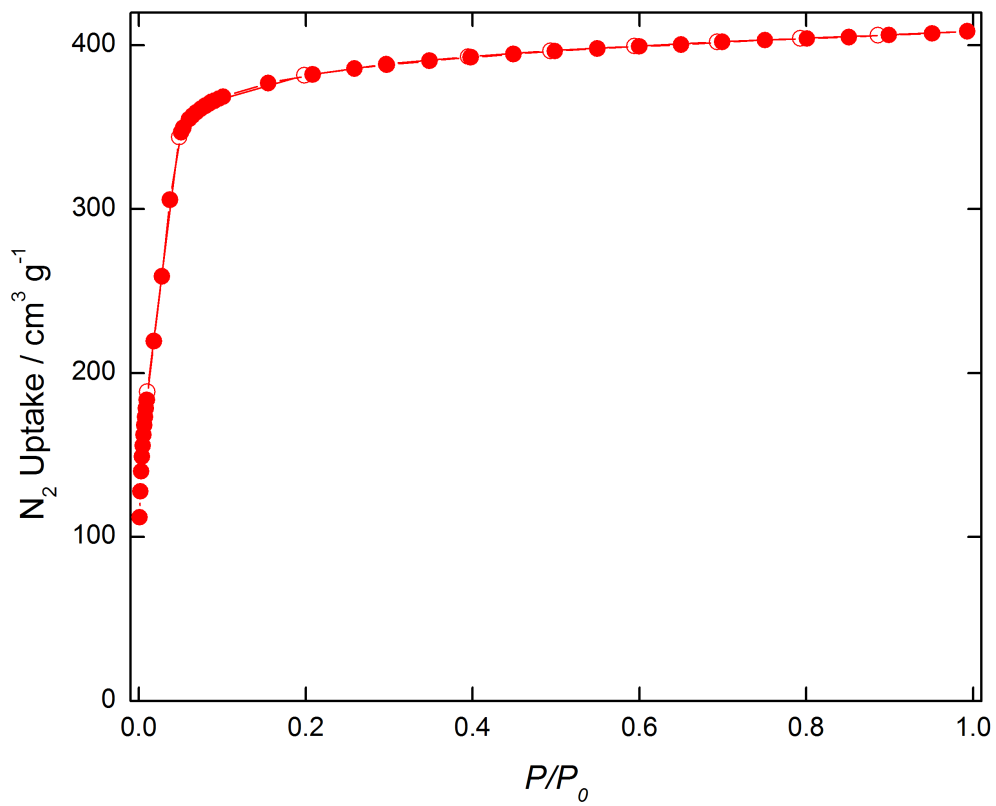


409

410 **Supplementary Figure 6.** N₂ adsorption isotherm of pristine MOF-808 at 77K.



411
412 **Supplementary Figure 19.** N₂ adsorption isotherms of MOF-808-SO₄ (blue circles) and dehydrated
413 MOF-808-SO₄ (red circles) at 77K.



414

415 **Supplementary Figure 20.** N₂ adsorption isotherm of at 77K.

416

417 Section 7: Solid State NMR Spectroscopy

418

419 **³¹P Solid State NMR experiments.** Samples for ³¹P Solid State NMR were prepared
420 following a slightly modified procedure based on the previously reported method (4). Briefly,
421 around 100 mg MOF sample was activated as described in Section 1, and 1.5 mL of 0.2 M
422 TMPO in chloroform was added and mixed with the MOF sample. This suspension was then
423 evacuated under dynamic vacuum at room temperature overnight, then at 50 °C for 8 hours. The
424 resulting solid was then packed into 75 uL Doty XC5 Kel-F sealing cells under argon
425 atmosphere, and inserted into a Doty 5 mm thin-wall zirconia rotor with Kel-F turbine caps.
426 Solid state NMR spectra were collected using a 7.05 T magnet with a Tecmag Discovery
427 spectrometer operating at 300.13 MHz for ¹H and 121.5 MHz for ³¹P. ³¹P chemical shifts were
428 externally referenced to aqueous H₃PO₄ (85%) at 0 ppm. Experiments were performed on a Doty
429 5-mm triple resonance MAS probe operating in ¹H/³¹P/⁸⁷Sr mode. Magic angle spinning (MAS)
430 was used to collect high resolution NMR spectra at a spinning rate of 8 kHz. ³¹P NMR
431 experiments were performed with a ³¹P 90° pulse time of 6 μs and a continuous wave ¹H
432 decoupling B₁ field of 60 kHz. Spectra were collected with a recycle delay time of 11 s, and were
433 processed with 5 Hz line broadening.

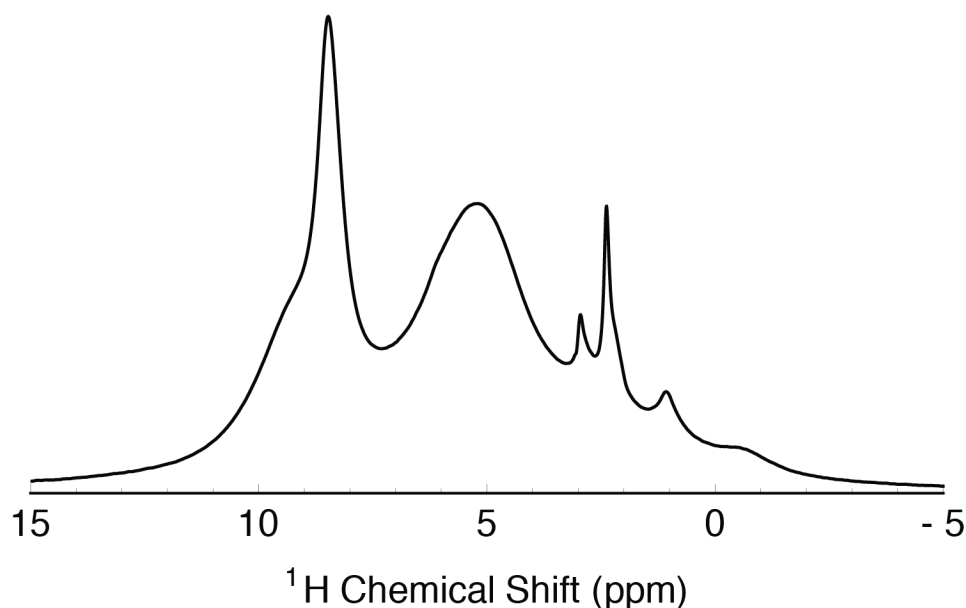
434 **¹H Solid State NMR experiments.** For direct ¹H MAS experiments, samples of MOF-
435 808-SO₄ and dehydrated MOF-808-SO₄ were packed into Doty 5 mm thick-wall zirconia rotors
436 with Kel-F turbine caps under argon atmosphere. Solid state NMR spectra were collected using a
437 7.05 T magnet with a Tecmag Apollo spectrometer operating at 300.27 MHz for ¹H. ¹H chemical
438 shifts were externally referenced to TMS at 0 ppm. Experiments were performed on a Doty 5-
439 mm triple resonance MAS probe. Magic angle spinning (MAS) was used to collect high
440 resolution NMR spectra at a spinning rate of 6 kHz. Pulse-acquire ¹H NMR experiments were
441 performed with a ¹H 90° pulse time of 4 μs and a recycle delay time of 5 s. The ¹H back-to-back
442 (BABA) rotor-synchronized DQ recoupling experiment was run at 11.74 T field using a Bruker
443 AV-500 spectrometer operating at 500.2 MHz for ¹H. The experiment was performed using a
444 Bruker 4 mm CP-MAS probe at an MAS rate of 12.5 kHz, with a 4 μs ¹H 90° pulse time and
445 recorded using two rotor period cycles with the BABA sequence for excitation and reconversion
446 of the double quantum coherences. Spectra were processed without apodization.

447 The MOF-808-SO₄ system differs from typical organic molecular solids in that there is
448 not a dense network of protons. The majority of proton-proton distances on a single zirconium
449 cluster are greater than 2 Å, and distance between clusters imposed by the MOF framework
450 reduces the influence of long-range homonuclear dipolar couplings. The spin interactions in this
451 system thus approach the limit of isolated two-spin dipolar couplings, which can be easily
452 resolved with magic-angle spinning (MAS) even at relatively low spinning rates.

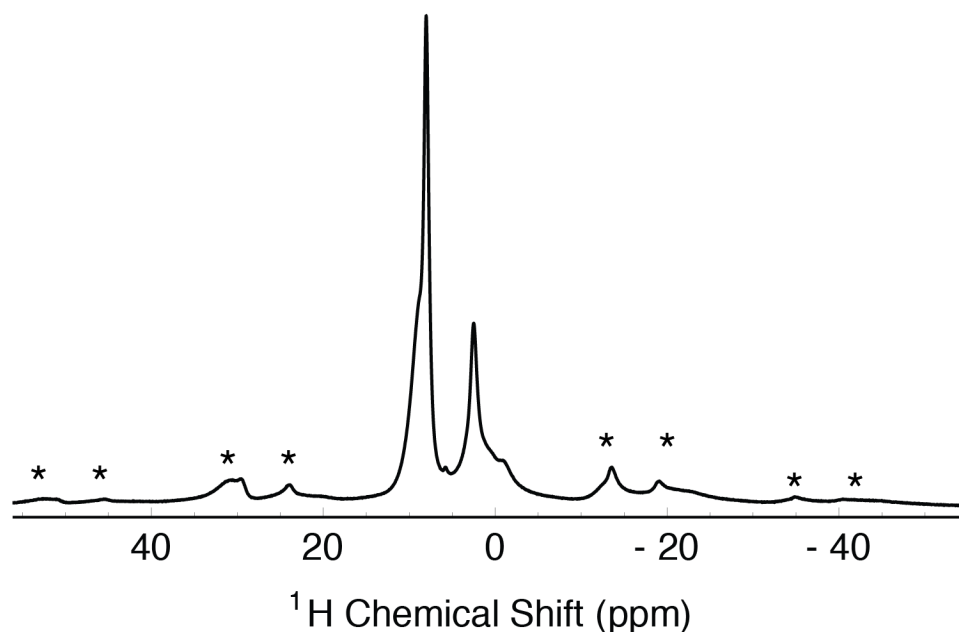
453 **¹H NMR Chemical shift calculations.** The NMR chemical shielding tensors for the
454 atoms in two of the DFT structure-optimized clusters were calculated using mPW1PW91 and the
455 default gauge-independent atomic orbital (GIAO) method available in Gaussian 09 with the basis
456 set 6-311++G(2d,2p) for all atom types excluding Zr, for which the basis lan12dz, 5d, 7f was
457 used (7 - 9). ¹H chemical shifts were referenced to tetramethylsilane, for which the structure and
458 NMR shifts were calculated at the same level of theory. No scaling factor was applied to the ¹H
459 chemical shifts, and as such we expect significant deviation from experimentally observed shifts;
460 instead the relative magnitudes of, and differences between, the calculated shift values were used
461 as a tool to inform the assignment of peaks in the experimental ¹H NMR results.

462

463 Exposure to atmospheric moisture (approximately 50% RH at 20 °C) also results in the
464 loss of acidity as observed previously (4), meaning water is a key component in the acidic
465 properties of MOF-808-SO₄, but not when it is in excess. This observation in MOF-808-SO₄ is
466 consistent with the proposition that the acid catalysis of its analogue, sulfated zirconia, only
467 operates in a specific humidity range (10). Supplementary figure 21 shows a ¹H NMR spectrum
468 after exposure to atmospheric moisture. There is a broad resonance centered about 5.2 ppm
469 which we assign as adsorbed water. The presence of this excess water should level the material's
470 acidity to the acidity level of the hydronium ion. As the resonance of bulk water is 4.8 ppm, the
471 slight upfield shift could be due to a lowering of the pH of the adsorbed water by some
472 deprotonation of the active site. Several other new peaks are present in the spectrum of the
473 hydrated MOF, which are likely protons in new hydroxide and adsorbed water species resulting
474 from the introduction of water vapor, but it is difficult to assign them precisely.
475



476
477 **Supplementary Figure 21.** Plot of the ¹H NMR spectra of MOF-808-SO₄ exposed to atmospheric
478 moisture (approximately 50% RH at 20 °C).
479



480

481 **Supplementary Figure 22.** Plot of the ^1H NMR spectra of MOF-808- SO_4 seen in main text figure
 482 5a, but displayed with the frequency range extended to show the manifold of spinning sidebands
 483 (denoted by asterisks).

484

485 **Supplementary Table 4.** Calculated ^1H NMR Chemical Shifts for ‘2wopp_optS,’ a cluster model
 486 with two chelating sulfates with adjacent water molecules

Atom Label	Chemical Group	Chemical Shift (ppm)	Notes
18	$\mu^i\text{-OH}$	9.3889	H-bonded to a chelating SO_4
23	$\mu^i\text{-OH}$	5.7650	Adjacent to H_2O but not H-bonded
26	$\mu^i\text{-OH}$	5.1614	Isolated on cluster
34	$\mu^i\text{-OH}$	2.8991	Enclosed between the three terminal acetates at the end of the cluster
52	$\mu^i\text{-OH}$	7.1503	
53	$\mu^i\text{-OH}$	6.2171	
54	H_2O	13.7517	Strongly H-bonded to a chelating SO_4 , and SO_4 is H-bonded to 18, aka “ H_a ” in the acid site
74	H_2O	4.6606	On H_2O with 54, aka “ H_b ” in the acid site
79	H_2O	5.6023	On H_2O with 80, aka “ H_c ” in the

acid site

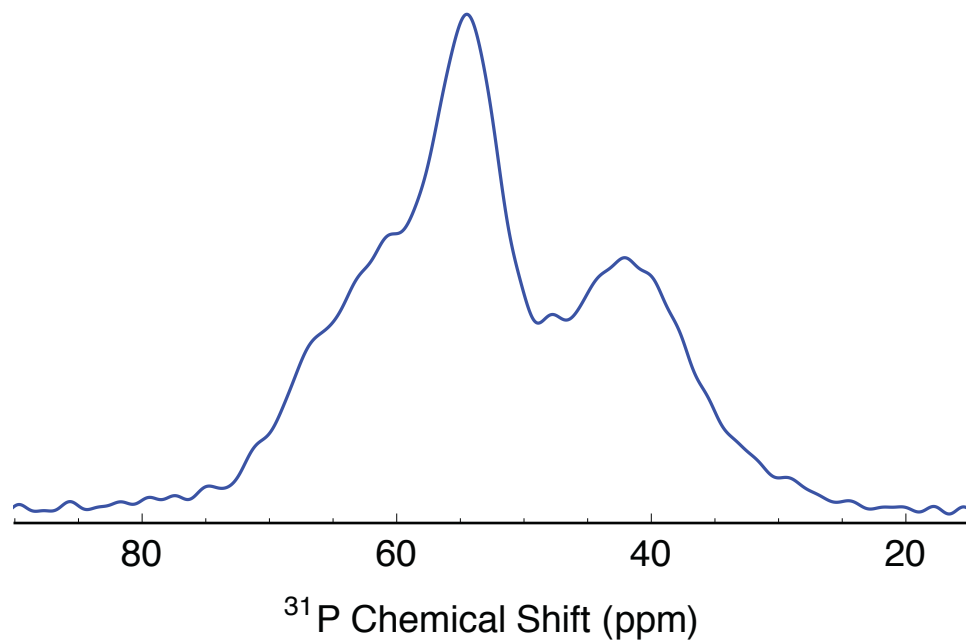
80	H ₂ O	10.7284	Strongly H-bonded to a chelating SO ₄ , which itself has no H-bond to μ-OH, aka "H _a " in the acid site
----	------------------	---------	---

487

488 **Supplementary Table 5.** Calculated ¹H NMR Chemical Shifts for '2opthighS,' a cluster model
489 with one bridging and one chelating sulfate, and one adsorbed water molecule.

Atom Label	Chemical Group	Chemical Shift (ppm)	Notes
21	μ ³ -OH	9.4348	H-bonded to chelating SO ₄
26	μ ³ -OH	10.0635	H-bonded to bridging SO ₄
29	μ ¹ -OH	5.4765	
37	μ ³ -OH	3.1569	Enclosed between the three terminal acetates at the end of the cluster
54	μ ¹ -OH	5.0904	
55	μ ¹ -OH	10.979	Partial H-bond to SO ₄
76	H ₂ O	3.2215	On H ₂ O with 77
77	H ₂ O	5.2524	Adjacent to bridging SO ₄

490



491

492 **Supplementary Figure 23.** Plot of the ^{31}P NMR spectra of trimethylphosphine oxide (TMPO)
493 adsorbed into MOF-808- SeO_4 . Though not as prominent as the peak at 69 ppm for MOF-808- SO_4
494 (Main text figure 3), there is signal intensity in the region of 60-70 ppm, suggesting the presence
495 of strong acid sites in MOF-808- SeO_4 . The peak centered at 42 ppm is due to excess TMPO that
496 is not interacting with acid sites directly. Other peaks in the spectrum belong to TMPO adsorbed
497 at various $\mu^1\text{-OH}$, $\mu^3\text{-OH}$, and water sites.

498

499

500 Section 8: Infrared Absorption Spectroscopy

501

502 Infrared (IR) absorption spectra of activated and dehydrated MOF samples were
503 measured in transmission mode on a Thermo Scientific Nicolet 6700 FTIR spectrometer with a
504 resolution of 1 cm^{-1} . The sample cell assembly process was performed in a N_2 glove box. A
505 minute amount of the MOF powder sample was sandwiched between two CaF_2 windows to form
506 a thin layer of 100 microns. The sample thickness was controlled by a Teflon spacer. Then the
507 windows with the sample were assembled into a gas-tight IR sandwich sample cell to seal. After
508 the assembly, the sample cell can be taken outside of the glove box without being compromised
509 by moisture in air. The sample cell was then transferred to the measurement chamber of the
510 FTIR spectrometer purged with CO_2 -free dry air. The background spectrum was simply taken on
511 the CO_2 -free dry air for calculating the absorbance. Since the sample spectra were acquired in
512 transmission mode on a powder sample, a large offset due to scattering is present in all the
513 measurements.

514 Infrared spectroscopy of MOF-808- SO_4 before and after dehydration reveals changes in
515 the region associated with O-H vibrations, where at least seven O-H stretches are observed in the
516 spectral region of 3550-3800 cm^{-1} (Supplementary figures 24, 25). Prior to dehydration, there is a
517 group of overlapping peaks in the range of 3550-3725 cm^{-1} , and two more distinct stretches
518 located at 3737 and 3767 cm^{-1} . After dehydration, these two peaks at 3737 and 3767 cm^{-1} are no
519 longer present, indicating that they originate from O-H vibrations belonging to adsorbed water.
520 We assign the peaks in the range of 3550-3725 cm^{-1} as O-H vibrations belonging to various μ -
521 OH and μ -OH groups. The strong blue shift of two O-H stretches at 3737 and 3767 cm^{-1} is
522 characteristic of exposed hydroxyl groups not participating in hydrogen bonding (11, 12). One of
523 these two peaks must belong to the O-H_s stretch in the acid site, while the other is likely an
524 asymmetric stretching mode for terminal water not participating in a hydrogen bond to chelating
525 sulfate. Our assignments are consistent with DFT calculations for the vibrational modes of our
526 modeled clusters which were done using M06-L in Gaussian 09 with the basis set 6-31+G(d,p)
527 for all atom types excluding Zr, for which the basis lan12dz, 5d, 7f was used (9,13,14). The
528 values for the O-H_s vibrational frequencies were calculated to be within 100-200 cm^{-1} of the
529 peaks associated with O-H vibrations on water not participating in a hydrogen bond. However,
530 the values for O-H_s vibrations were calculated to be present 1000-1500 cm^{-1} lower than the O-H_s
531 vibrations. The O-H_s vibration should be located at a lower frequency due to the hydrogen
532 bonding interaction with sulfate. However, no absorption features between 2000-3500 cm^{-1} were
533 observed in the experiment that were not otherwise attributable to C-H modes on the BTC linker,
534 due to a low signal to noise ratio (Supplementary figure 24b). We believe that the O-H_s vibration
535 likely is not at such a low frequency as calculated by DFT, but rather may be present in the
536 region between 3550-3725 cm^{-1} . However, due to the large degree of overlapping peaks in the
537 region below 3700 cm^{-1} , it is difficult to see changes in this region after the water loss, but the
538 presence of these blue-shifted O-H stretches and their subsequent loss after dehydration is
539 consistent with our proposed Brønsted acid site.

540

541

542 **Supplementary Table 6.** Calculated IR frequencies for O-H vibrational modes in '2wopp_optS,' a
543 cluster model with two chelating sulfates with adjacent water molecules.

Frequency (cm^{-1})	Chemical Group primarily associated with the calculated vibrational mode
--------------------------------	--

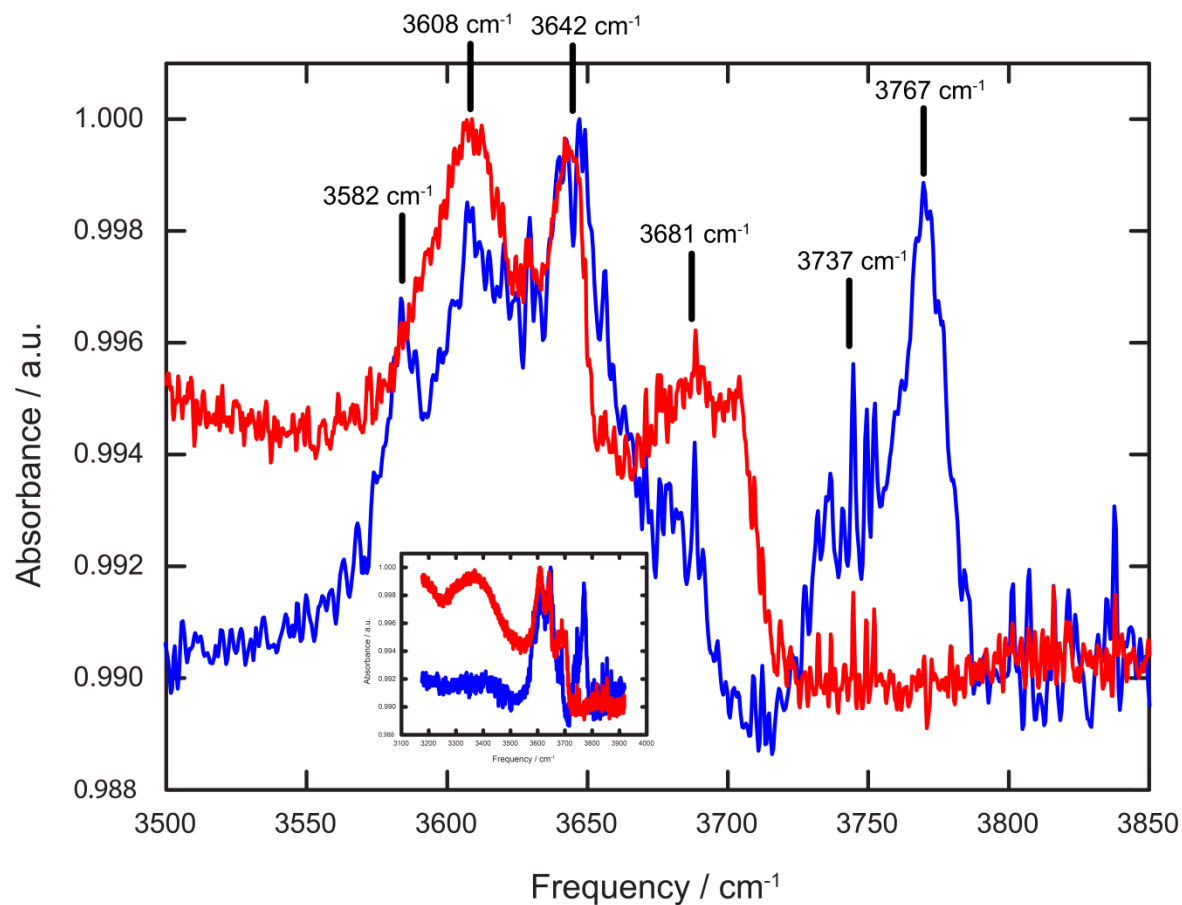
3779	μ -OH
3747	μ -OH
3745	μ -OH
3718	μ -OH
3679	μ -OH
3657	O-H _s on H ₂ O for site 1
3588	O-H _s on H ₂ O for site 2
3220	μ -OH
2988	O-H _i on H ₂ O for site 2
2604	O-H _i on H ₂ O for site 1

544

545 **Supplementary Table 7.** Calculated ¹H NMR Chemical Shifts for ‘2opthighS,’ a cluster model
546 with one bridging and one chelating sulfate, and one adsorbed water molecule.

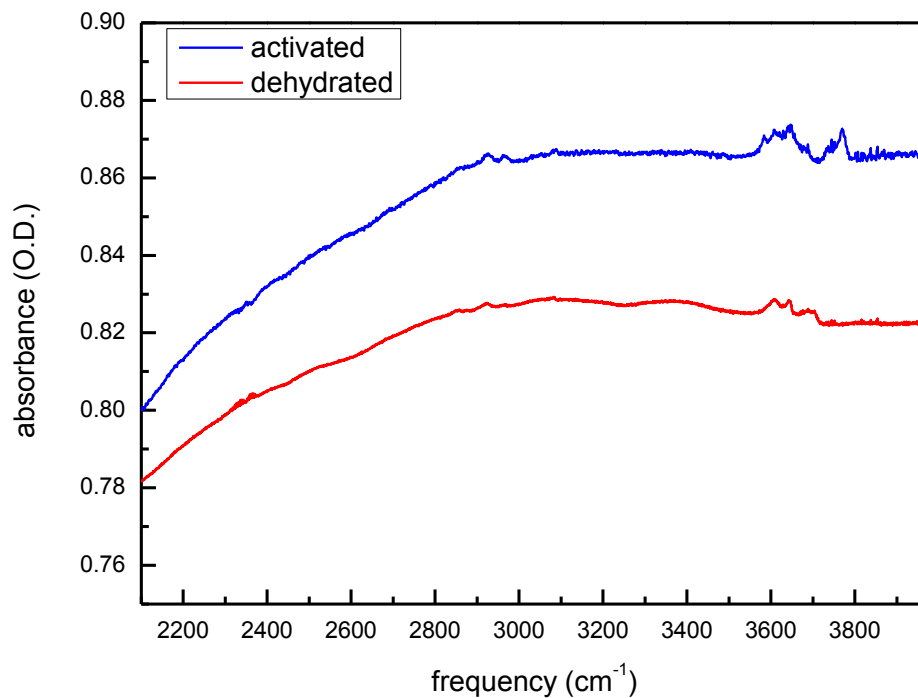
Frequency (cm ⁻¹)	Chemical Group primarily associated with the calculated vibrational mode
3824	μ -OH
3780	μ -OH
3766	μ -OH
3750	Asymmetric stretch H ₂ O
3532	μ -OH
3526	Symmetric stretch H ₂ O
3241	μ -OH
3223	μ -OH

547



548

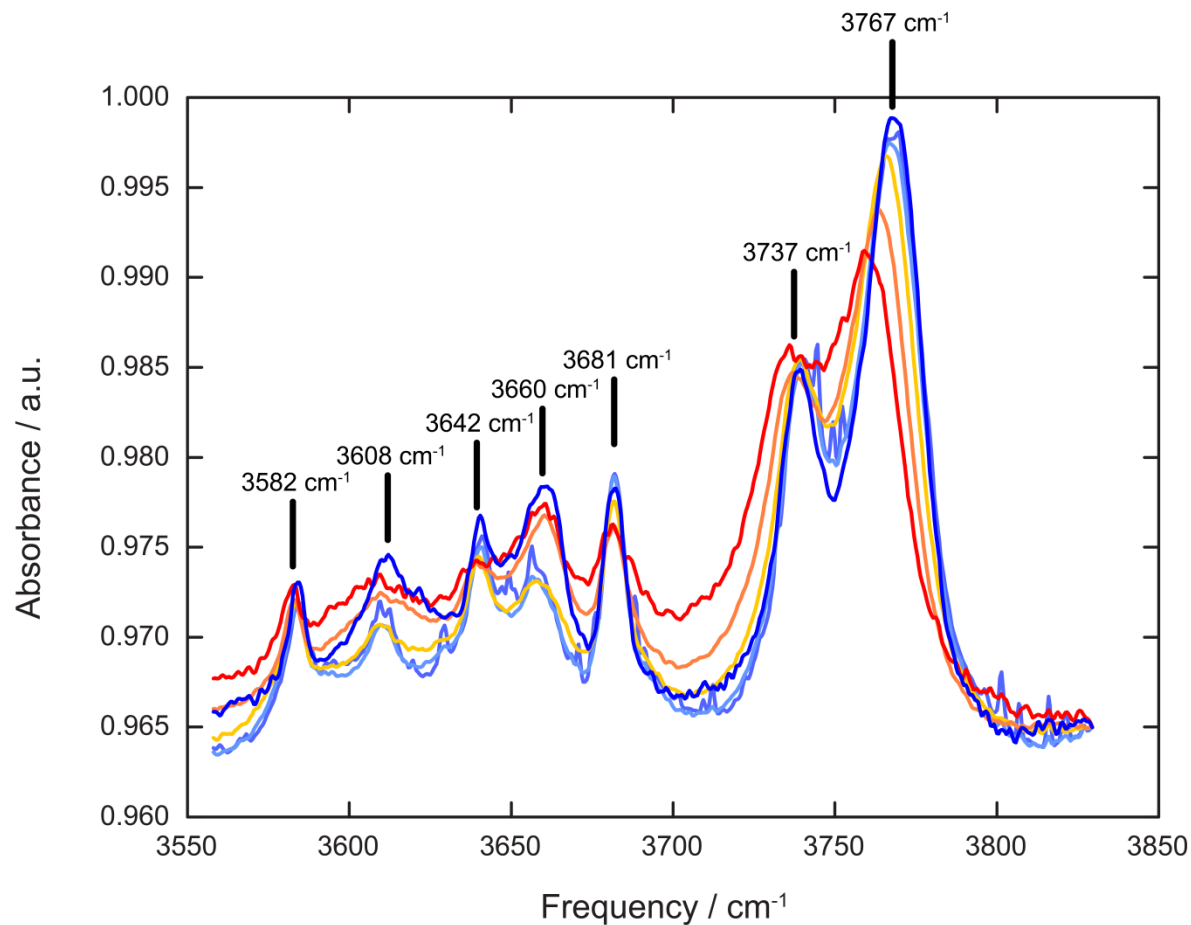
549 **Supplementary Figure 24a.** A comparison of the IR spectra of activated (blue) and dehydrated (red)
 550 stages of MOF-808-SO₄ in the spectral region relevant to O-H stretches. The most notable feature is the
 551 loss of the two blue-side peaks at 3737 and 3767 cm⁻¹. The inset is included to show the broad feature
 552 centered around 3350 cm⁻¹ in the dehydrated structure, which corresponds to a minute amount of water
 553 adsorbed onto the MOF-808-SO₄ crystals.



554

555 **Supplementary Figure 24b.** Expanded range IR spectra shown in supplementary figure 24a, showing the
556 lack of distinct features between 2000-3000 cm⁻¹ that cannot otherwise be attributed to aromatic C-H
557 vibrational modes of the linker, and the low signal-to-noise in the region between 3000-4000 cm⁻¹ that was
558 characteristic of our IR studies for multiple batches of this material.

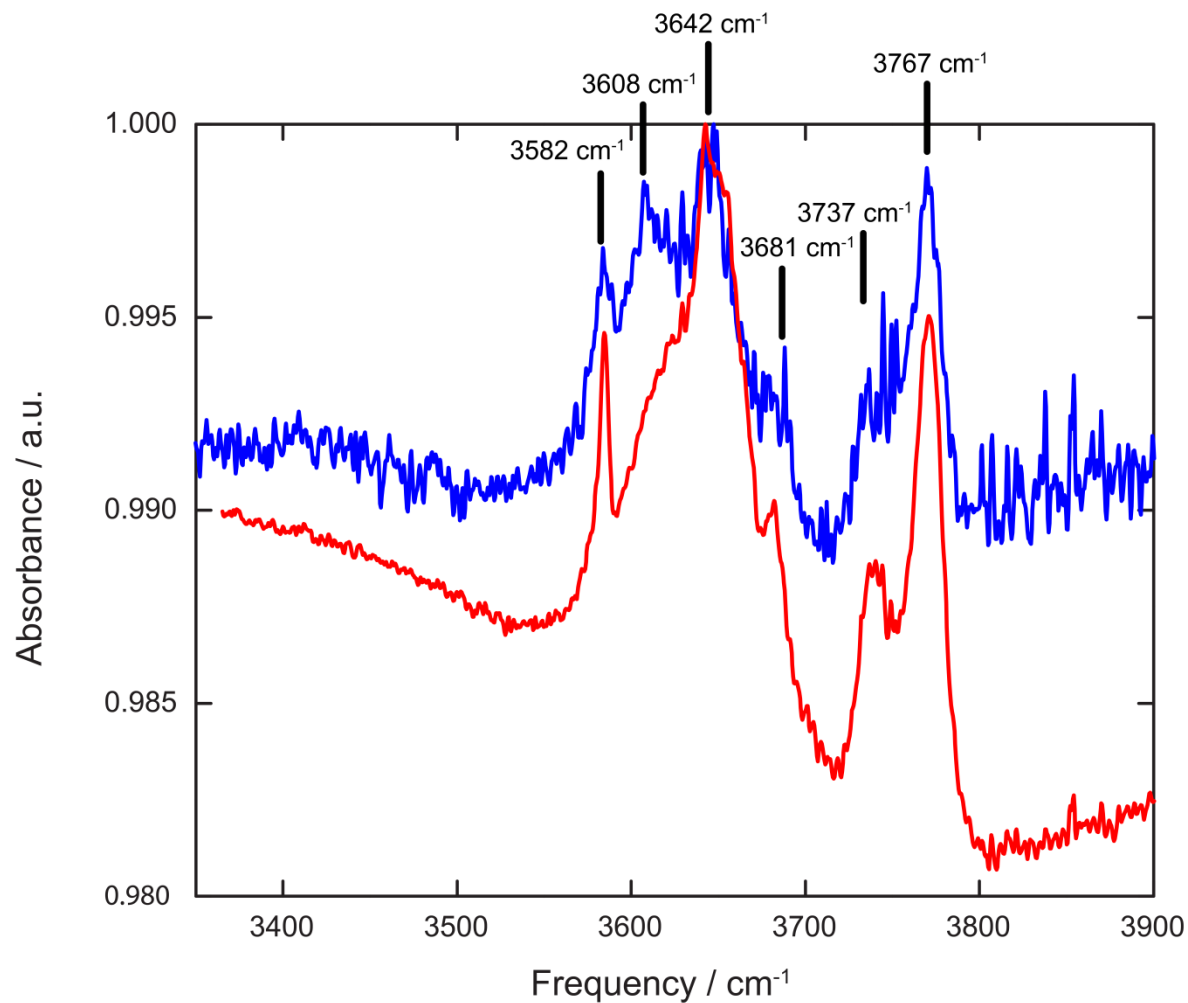
559



560

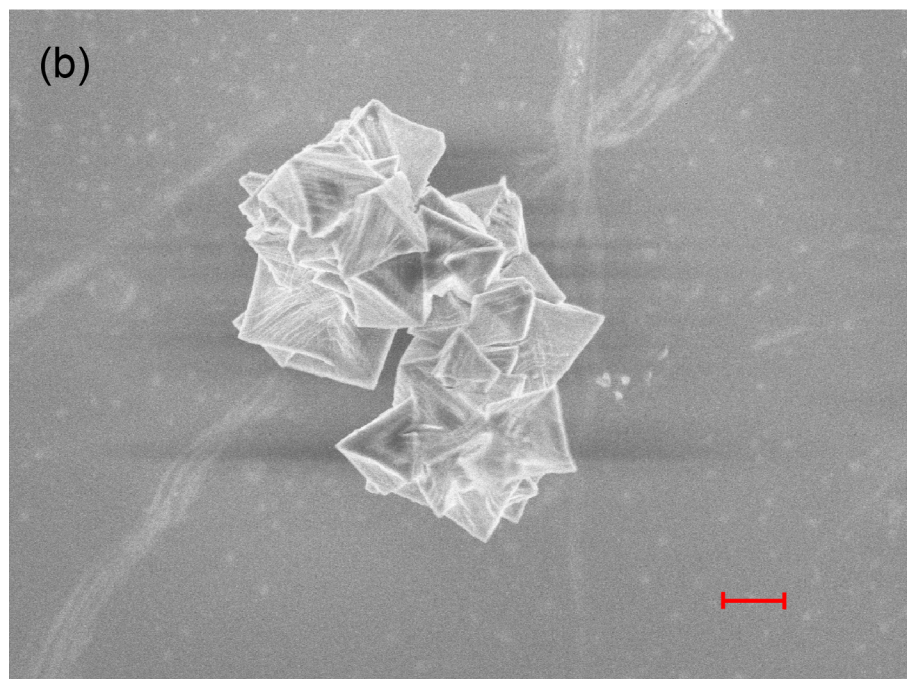
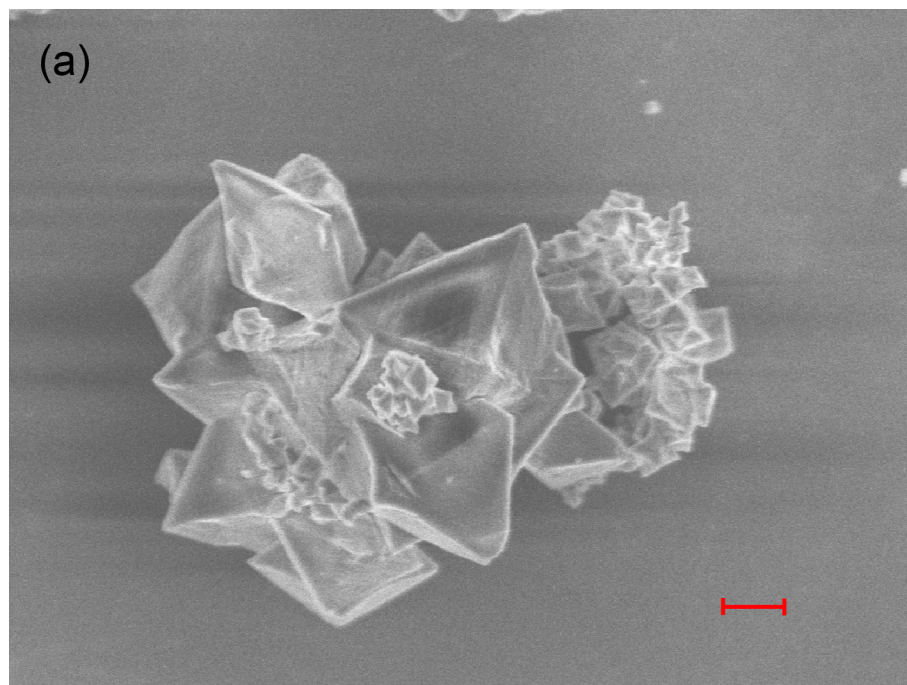
561 **Supplementary Figure 25.** A comparison of the IR spectra of a different batch (compared to
 562 supplementary figure 24) of activated MOF-808-SO₄ measured at different temperatures. Heating the
 563 sample broadens the peaks as the local environment becomes more disordered due to thermal motion. The
 564 process is reversible between room temperature and 200 °C. The measurement was started at room
 565 temperature (light blue) then heated gradually to 40 °C (light purple), 80 °C (yellow), 125 °C (orange),
 566 200 °C (red), and cooled back down to room temperature (dark blue).

567



568
 569 **Supplementary Figure 26.** A comparison of the *in situ* IR spectra of activated MOF-808-SO₄ (blue) and
 570 MOF-808-SeO₄ (red) in the energy region relevant to O-H stretches. Both samples display the same O-H
 571 stretch features, indicating the water and hydroxide environments in both samples are similar.

572
 573
 574
 575
 576
 577
 578
 579



582
583 **Supplementary Figure 27.** Scanning electron microscope (SEM) images of (a) MOF-808-SO₄ and (b)
584 MOF-808-SeO₄ following activation under dynamic vacuum at 120 °C (scale bar 1 μm).

587 Cluster optimizations were performed and geometrically optimized using density
588 functional theory (DFT), based on the formula $Zr_6O_4(OH)_4(C_2H_3O_2)_6(SO_4)_2(OH)_2(OH_2)_x$, where $x = 2$
589 or 3. Acetate groups were used instead of BTC as a terminal ligand. The functional B97-D3 was
590 chosen, which is the B97 functional with Grimme's dispersion term added on to account for
591 dispersive effects that B97 misses. The chosen basis set was 6-31G* for all non-Zr atoms. For
592 Zr, the CRENBL effective core potential was used for core electrons, with the matching
593 CRENBL basis for valence electrons. A very fine grid consisting of 90 radial points and 590
594 angular points was selected for the numerical integration step to account for exchange-
595 correlation. Early evaluation of cluster models by classical force field geometry optimization
596 followed by energy calculation found that an uneven distribution of charge or chemical species
597 resulted in much higher energy configurations, or even failed to converge. For instance, a
598 configuration where two hydroxides are localized on one zirconium atom and two open metal
599 sites are assigned to another was 300-400 kJ mol⁻¹ higher in energy than both zirconium atoms
600 assigned a single hydroxide group each, depending on the exact configuration.
601

602

603 Section 11: Acid Catalysis of Isobutene

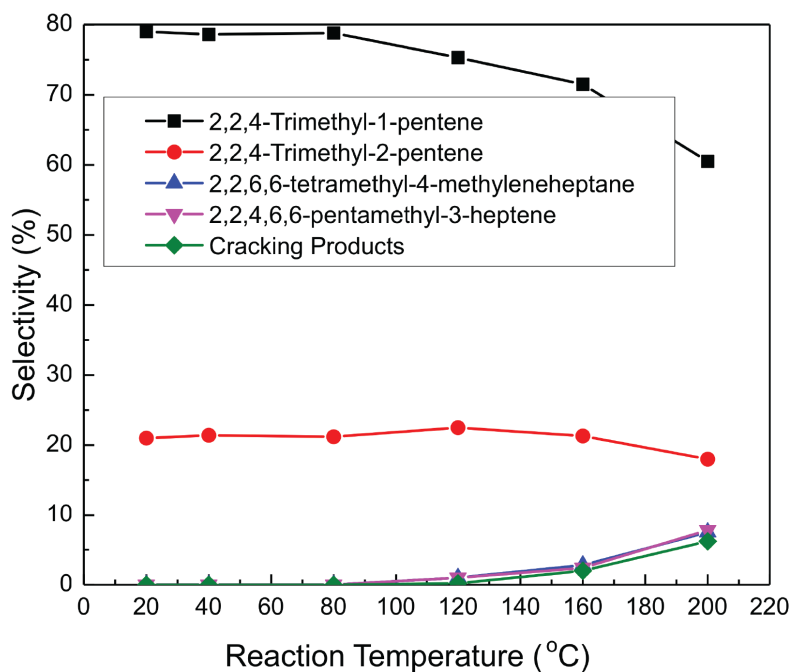
604

605 A flow reactor set-up was used to test the catalytic performance of various acid catalysts:
606 H-ZSM-5 (ammonium type, Si/Al ratio 20/1, Alfa Aesar), Amberlyst (Sigma Aldrich) and
607 sulfated zirconia. Sulfated zirconia was prepared as explained in section 1. Gas feeds of 2 mL
608 min⁻¹ isobutene and 20 mL min⁻¹ He regulated by a mass flow controller to be at 1 atm, were
609 mixed together and directed towards the catalyst (90 mg), loaded into a tube furnace. The
610 temperature of the catalyst bed was monitored by a K-type thermocouple controlled by a PID
611 controller. The products were analyzed using an HP 6890 series GC-MS with a Supelco column
612 (phase 23% SP-1700 support, 80/100 chromosorb PAW). Since the number of acid sites for each
613 catalyst is unknown, the catalysts were compared by mass. The conversion and selectivity of
614 isobutene and isoctene were calculated using the following equations:

$$\text{Isobutene conversion (\%)} = \frac{\text{Isobutene}_{\text{in}} - \text{Isobutene}_{\text{out}}}{\text{Isobutene}_{\text{in}}} \times 100$$

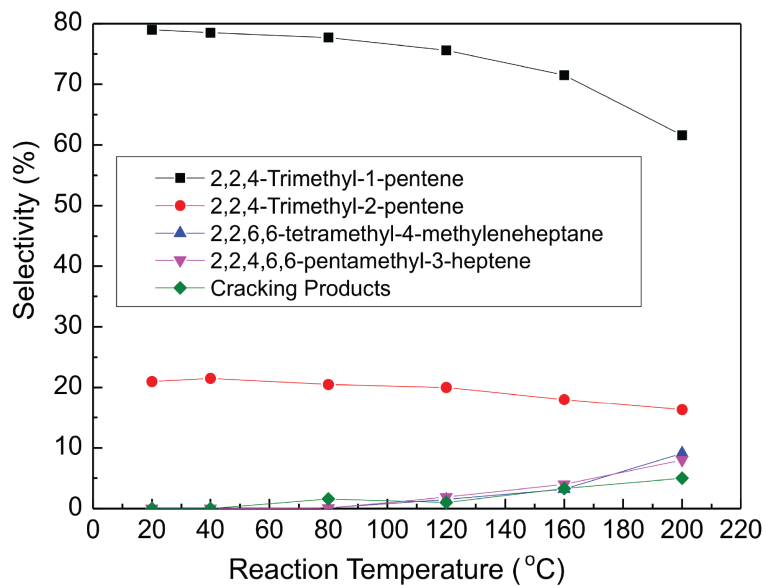
$$\text{Isooctene selectivity (\%)} = \frac{n_{\text{Isooctene}}}{n_{\text{Dimers}} + n_{\text{Trimers}}} \times 100$$

615 where n is number of hydrocarbons in moles.

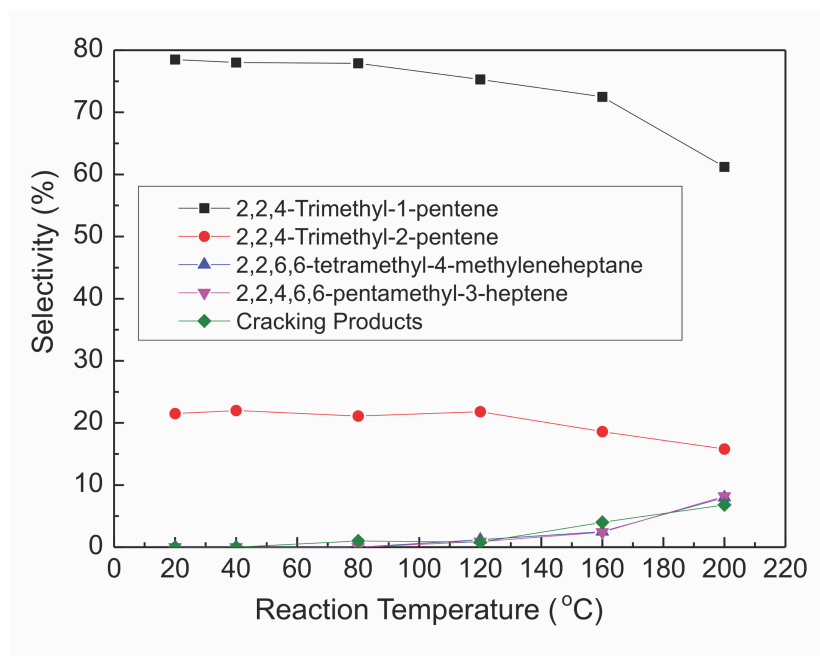


616

617 **Supplementary Figure 28.** Product distribution for the dimerization of isobutene using MOF-808-SO₄.



618
 619 **Supplementary Figure 29.** Product distribution for the dimerization of isobutene using dehydrated
 620 MOF-808-SO₄.
 621



622
 623 **Supplementary Figure 30.** Product distribution for the dimerization of isobutene using sulfated zirconia.
 624

625 **Section 12: References**

- 626 1. Bruker, in *APEX2 (Bruker AXS Inc., Madison, Wisconsin, U.S.A)* (2010).
- 627 2. G. M. Sheldrick, A short history of SHELX. *Acta Crystallogr. Sect. A Found. Crystallogr.*
628 **64**, 112–122 (2007).
- 629 3. O. V. Dolomanov, L. J. Bourhis, R. J. Gildea, J. A. K. Howard, H. Puschmann, OLEX2:
630 A complete structure solution, refinement and analysis program. *J. Appl. Crystallogr.* **42**,
631 339–341 (2009).
- 632 4. J. Jiang *et al.*, Superacidity in Sulfated Metal – Organic Framework-808. *J. Am. Chem.*
633 *Soc.* **136**, 12844–12847 (2014).
- 634 5. X. Song and A. Sayari., Sulfated zirconia-based strong solid-acid catalysts: recent
635 progress. *Catalysis Reviews* **38**, 329-412 (1996).
- 636 6. TOPAS 5. *Bruker AXS, Madison, WI, USA.*
- 637 7. R. Krishnan, J. S. Binkley, R. Seeger, J. A. Pople, Self-consistent molecular orbital
638 methods. XX. A basis set for correlated wave functions. *J. Chem. Phys.* **72**, 650–654
639 (1980).
- 640 8. J. Struppe, Y. Zhang, S. Rozovsky, ⁷⁷Se chemical shift tensor of L-selenocystine:
641 Experimental NMR measurements and quantum chemical investigations of structural
642 effects. *J. Phys. Chem. B.* **119**, 3643–3650 (2015).
- 643 9. Gaussian 09, Revision D.01, M. J. Frisch, G. W. Trucks, H. B. Schlegel, G. E. Scuseria,
644 M. A. Robb, J. R. Cheeseman, G. Scalmani, V. Barone, G. A. Petersson, H. Nakatsuji, X.
645 Li, M. Caricato, A. Marenich, J. Bloino, B. G. Janesko, R. Gomperts, B. Mennucci, H. P.
646 Hratchian, J. V. Ortiz, A. F. Izmaylov, J. L. Sonnenberg, D. Williams-Young, F. Ding, F.
647 Lipparini, F. Egidi, J. Goings, B. Peng, A. Petrone, T. Henderson, D. Ranasinghe, V. G.
648 Zakrzewski, J. Gao, N. Rega, G. Zheng, W. Liang, M. Hada, M. Ehara, K. Toyota, R.
649 Fukuda, J. Hasegawa, M. Ishida, T. Nakajima, Y. Honda, O. Kitao, H. Nakai, T. Vreven,
650 K. Throssell, J. A. Montgomery, Jr., J. E. Peralta, F. Ogliaro, M. Bearpark, J. J. Heyd, E.
651 Brothers, K. N. Kudin, V. N. Staroverov, T. Keith, R. Kobayashi, J. Normand, K.
652 Raghavachari, A. Rendell, J. C. Burant, S. S. Iyengar, J. Tomasi, M. Cossi, J. M. Millam,
653 M. Klene, C. Adamo, R. Cammi, J. W. Ochterski, R. L. Martin, K. Morokuma, O. Farkas,
654 J. B. Foresman, and D. J. Fox, Gaussian, Inc., Wallingford CT, (2016).
- 655 10. D. Fraenkel, Acid Strength of Sulfated Zirconia Inferred from Catalytic Isobutane
656 Conversion. *Chem. Lett.* **9**, 917–918 (1999).
- 657 11. E. Libowitzky, Correlation of O-H Stretching Frequencies and O-H-O Hydrogen Bond
658 Lengths in Minerals. *Monatsh. Chem.* **130**, 104-115 (1999).

- 659 12. C. Yan, J. Nishida, R. Yuan, M.D. Fayer, Water of Hydration Dynamics in Minerals
660 Gypsum and Bassanite: Ultrafast 2D IR Spectroscopy of Rocks. *J. Am. Chem. Soc.* **138**,
661 9694-9703, (2016).
- 662 13. J.C. Howard, J.D. Enyard, G.S. Tschumper, Assessing the accuracy of some popular DFT
663 methods for computing harmonic vibrational frequencies of water clusters. *J. Chem. Phys.*
664 **143**, 214103, (2015).
- 665 14. I. M. Alecu, J. Zheng, Y. Zhao, and D. G. Truhlar, Computational Thermochemistry:
666 Scale Factor Databases and Scale Factors for Vibrational Frequencies Obtained from
667 Electronic Model Chemistries, *J. Chem. Theory Comput.* **6**, 2872-2887, (2010).